Understanding Capacity Sensitivity of Cooled Transonic Nozzle Guide Vanes: A Parametric Experimental and Computational Study of the Impact of Trailing Edge Geometry

Daniel Burdett
Department of Engineer Science,
University of Oxford,
Oxford OX2 0ES, UK
e-mail: daniel.burdett@univ.ox.ac.uk

Frédéric Goenaga
Rolls-Royce plc,
WH88, P.O. Box 3,
Filton BS34 7QE, UK
e-mail: Frederic.Goenaga@rolls-royce.com

Thomas Povey[1]
Department of Engineering Science,
University of Oxford,
Oxford OX2 0ES, UK
e-mail: thomas.povey@eng.ox.ac.uk

High-pressure (HP) nozzle guide vane (NGV) capacity is one of the most important parameters for setting overall turbine power output, for stage matching, and for understanding turbine performance. Accurate capacity prediction early in the engine design process reduces the cost and risk of late-stage changes in the overall turbine design. High accuracy predictions rely on calibrated computational fluid dynamics (CFD) methods. Because of the numerous sensitivities in the methods, they are generally restricted to certain classes of design for which there is experimental validation. This paper considers the effect of changes in trailing edge (TE) geometry—particularly suction side (SS) TE overhang length—on the flow capacity of a modern HP NGV. Ultra-low uncertainty experimental measurements and complementary numerical predictions of capacity are presented for four TE geometries, in a parametric study bridging the gap between a classical centered-ejection design and a SS overhang TE design. This study discusses the absolute and relative (differences between designs) accuracies of the numerical method and develops understanding of the sensitivity of capacity to TE geometry. Fundamental mechanisms responsible for the observed capacity changes are elaborated. The impacts on capacity of both changes in the coolant flows and the boundary layers in the controlling region of the vane passage are considered. These effects are found to be very small. A simple total pressure loss model was also developed but was found to be a poor predictor of the observed capacity changes across the entire range of overhang lengths. To understand the observed changes, two more sophisticated models of the vane passage are proposed. In the first model—for relatively long TE overhangs—the mainstream and TE flows (and a wake) pass through a common minimum area. In the second model—for relatively short TE overhangs—the two flows are considered to pass through independent, non-interacting minimum areas. This framework reconciles the experimental and numerical data with the models but illustrates the complexity of the problem. In particular, it demonstrates the arbitrariness of considering a single minimum area. Contrary to some received industrial wisdom, it is argued that deemphasising this construct, and explaining capacity changes by examining aerodynamic changes in the entire controlling region of the passage, is more helpful in attempting to understand design sensitivities. [DOI: 10.1115/1.4050068]

Keywords: computational fluid dynamics (CFD), fan, compressor, and turbine aerodynamic design, fluid dynamics and heat transfer phenomena in compressor and turbine components of gas turbine engines, measurement techniques, turbomachinery blading design

Introduction

Capacity provides a quasi-non-dimensional measure of the mass flowrate passing through a turbomachine row or stage. Accurate evaluation of high-pressure (HP) nozzle guide vane (NGV) capacity, in particular, is important to ensure well-matched turbine stages, correct compressor operating point, and accurate understanding of turbine performance parameters (efficiency, specific work, etc.). Capacity can be defined by

$$\Gamma = \frac{\dot{m}\sqrt{T_0}}{p_0} \tag{1}$$

While Eq. (1) is *not* strictly non-dimensional, it does remove the dependence of mass flowrate on the total pressure and temperature conditions at inlet to the nozzle. Designers typically require estimations of NGV capacity accurate to within 1% even at an early design stage. Evaluation at this accuracy level necessitates consideration of not just primary influencing factors such as vane loading

[1]Corresponding author.

Contributed by the Heat Transfer Division of ASME for publication in the JOURNAL OF TURBOMACHINERY. Manuscript received July 21, 2020; final manuscript received January 4, 2021; published online March 30, 2021. Assoc. Editor: James L. Rutledge.

distribution [1] and the development of energy loss in the vane surface boundary layers [2] but also secondary design features including 3D vane geometry (sweep, lean, endwall contouring, etc.), surface film cooling, trailing edge (TE) shape, TE coolant ejection, inlet conditions of swirl and turbulence intensity, platform steps, platform leakage, and so forth. Significant advances made in both experimental and numerical methods for low uncertainty capacity evaluation in recent years have made it possible to understand the impact of these secondary factors on NGV capacity.

High accuracy evaluation of NGV capacity requires a high technology readiness level (TRL) experimental setup. The use of a fully annular cascade of engine component NGV parts is necessary to ensure correct boundary conditions are supplied to the vane. The cascade must further be operated at appropriate non-dimensional conditions of Mach and Reynolds numbers. Traditionally, the operation of such high-TRL facilities has been limited to original equipment manufacturers due to the great expense which they entail. For this reason, there are very few studies of NGV capacity in the open literature—in contrast to its importance in the engine design process. To date, the work of the group involved in this paper is the only major program targeting low uncertainty experimental capacity measurement in an academic environment.

In 2011, Povey et al. [3] presented a novel experimental technique for capacity measurement in a semi-transient blowdown facility. This technique offered significant improvement in accuracy over conventional continuous-running techniques, with significant reductions in operating cost and test runtime. In 2017, the installation of a second-generation facility [4] extended the capability to include high-fidelity aerodynamic traverse measurements of the downstream flow field and overall cooling effectiveness measurements using infrared thermography, as well as a modular working section uniquely suited to measuring very small capacity changes arising from small vane geometry changes. Around the same time, Burdett et al. [5] implemented a number of small improvements to the hardware and experimental technique to allow ultra-low uncertainty capacity evaluation. This facility was used for the experimental work in this paper. Burdett et al. [5] provide a comprehensive uncertainty analysis. The development of these techniques and facilities has paved the way for sensitivity studies in which very small changes in flow capacity (of order 0.1% or lower) are to be studied.

In this paper, we consider the impact of suction side (SS) TE overhang on capacity. This type of design has evolved to afford a thinner TE (improved aerodynamic performance) with acceptable thermal life (controlled coolant ejection over the thin SS overhang). Because the overhang feature occurs in the *controlling region* (defined more fully later) of the vane passage, the vane capacity and loss are expected to be highly sensitive to the overhang design. Centered-ejection-type TE designs were common in earlier-generation engines because of the ease of cooling. More modern engine designs have favored TE designs with a SS overhang, as they are generally found to yield lower loss than equivalently optimized centered-ejection designs on account of their thinner *base region* [6,7]. However, recent evidence suggests that at lower exit Mach number conditions, the centered-ejection design may offer benefits from both aerodynamic and thermal perspectives. This is of particular interest to the development of current twin-HP engine designs and was the primary motivation for the present study.

In addition, deterioration of the TE overhang geometry can occur during the service lifetime of the NGV component. Impacts from foreign body particles passing through the engine core can result in significant removal of material from the TE tip. Attempts are commonly made to mitigate the effects of such deterioration by periodically removing damaged sections of the TE material across the whole vane span.

Accurate evaluation of capacity (to within approximately 1%) by numerical means is also challenging. It is first required to replicate faithfully the 3D geometry of the physical part. The geometry is commonly obtained either from a computer aided design (CAD) casting drawing of the nominal part (and therefore subject to deviation from a specific manufactured component due to tolerances in the casting process) or by employing optical scanning techniques (which encounter errors relating to the process of converting from a set of scanned points to a clean geometry which will then be meshed) to measure a physical part directly. The width of the passage in a typical HP NGV close to the region of minimum physical area is of order 10 mm. Therefore, a discrepancy in passage width in this area between the physical part geometry and the numerical mesh of just 0.1 mm would result in a capacity shift of order 1%. This demonstrates the small margin for error in the process of geometry and mesh generation.

Attempts to investigate and understand the effects of secondary geometry features only add to the difficulty. A fine mesh is required to resolve small-scale geometric features which can disproportionately impact the aerodynamic flow field. This naturally brings increased computational cost. At typical operating conditions, the flow field in the immediate vicinity of the controlling region is transonic (flow Mach number largely in the range $0.8 \leq M \leq 1.1$) and highly unsteady, generally featuring vortex shedding from the TE. Running unsteady simulations is therefore greatly advantageous and is usually considered a requirement for correctly determining the vane TE loss.

At the TE, there is a strong interaction between coolant flow ejecting from the TE slot and the external flow field around the TE. A mass flowrate boundary condition is typically imposed at inlet to the TE slot, varied between operating conditions (e.g., pressure ratio) and geometry to take account of the time mean pressure field in the so-called *base region*. The mass flow might be predicted using a low-order model of the system. In addition to boundary conditions, coolant ejection will also be influenced by internal cooling geometry features within the TE slot. Typically, these include ribs, pin-fins, and impingement plates which cause the TE ejection profile to be non-uniform over the vane span. It is therefore important that these features should be included in the numerical geometry, adding further complexity.

A small number of studies have employed numerical or theoretical methods to consider the influence of secondary factors on NGV capacity. These will now be summarized.

Afanasiev et al. [1] compared vanes with common minimum area but different loading distributions. A typical change in loading was found to alter capacity by up to 10%. Aft-loading can move the *controlling* minimum area well downstream of the *geometric* minimum area, where a simplistic 1D analysis would expect the flow to choke. This demonstrates the folly of attempting to understand small capacity discrepancies between vanes by considering their geometric throat areas alone—however accurately they are measured.

Povey [8] introduced a novel analytical model designed to predict the impact of film cooling on NGV capacity, using a control volume mixing model. The model was used to estimate a correction parameter between capacity at typical experimental test conditions and at engine conditions. Capacity differences between the conditions of order 1.88% are suffered when the mainstream properties are assumed for the whole flow. Alternatively, defining capacity using fully mixed out properties, the capacity difference could be reduced by an order of magnitude to approximately 0.20%.

Hambidge and Povey [9] developed this further by comparing theoretical and numerical predictions of the impact of film cooling on NGV capacity. The introduction of a typical film cooling system was estimated to reduce capacity by 0.125% or 0.144% using numerical and theoretical methods, respectively. They also showed that the impact on capacity is only weakly sensitive to the actual distribution of film cooling holes and is primarily determined by the overall coolant mass flowrate.

Högner et al. [10] numerically quantified the impacts on NGV capacity of a range of typical geometric variations which may arise due to manufacturing scatter. These included thickness and position of the TE slot, SS and pressure side (PS) TE overhang lengths, and pressure and suction surface offsets. The effects of typical variation in each aspect of geometry were estimated both

in isolation and in parallel (via a Monte Carlo simulation). The pressure surface offset and the position of the TE slot were identified as the primary influences on capacity. Simple linear superposition of these two parameters acting in isolation gave a comparable result to the parallel study, demonstrating a high degree of linearity and relative lack of cross-dependence.

In this paper, the impact of TE slot geometry on NGV capacity is examined using both experimental and numerical techniques. Specifically, we attempt to understand the effect of varying the overhang length of the SS TE tip (with respect to the PS TE tip). A series of four different TE geometries have been tested. These are presented along with the method by which they were manufactured in the experimental test cascade. The NGV capacity trend is quantitatively analyzed from the experimental and numerical results. Experimental measurements are used to validate the numerical method. Numerical results are then used to enhance understanding of the fundamental changes to the underlying flow field which give rise to the measured change in capacity.

Experimental Capacity Measurement

Experimental measurements were conducted in the Oxford Engine Component Aerothermal (ECAT) facility [4]. This facility utilizes the semi-transient method of experimental capacity measurement, first presented by Povey et al. in 2011 [3]. Burdett et al. [5] provide a comprehensive explanation of the application of the method in the ECAT facility and analyze the bias uncertainty in capacity measurements achieved. Bias uncertainty is evaluated as ±0.495% to 95% confidence.

Air, supplied from a HP reservoir, is discharged through a full-annular cascade of test vanes. The cascade was made up of 20 vane pairs (40 vanes in total) from a modern civil turbofan engine. Figure 1 shows a simplified cross section through the axisymmetric working section. Mainstream air flows from left to right in the figure. The test vanes feature distributed surface film cooling and coolant ejection from a TE slot. Coolant air is supplied from independent feeds at the hub and case.

The mainstream mass flowrate delivered to the cascade is accurately measured using a choked sonic Venturi nozzle calibrated to a National Institute of Standards and Technology (NIST) traceable standard at Colorado Engineering Experiment Station, Inc. (CEESI) and installed according to ISO 9300 [11]. Coolant mass flowrates are measured using independent sonic Venturi nozzles. The coolant metering nozzle area sets the coolant-to-mainstream inlet total pressure ratio. Figure 2(*a*) shows the mainstream, coolant, and overall (mainstream + coolant) mass flow trends from a typical test. The mainstream trend is truncated at the start and end of the test, where the pressure ratio across the metering nozzle is

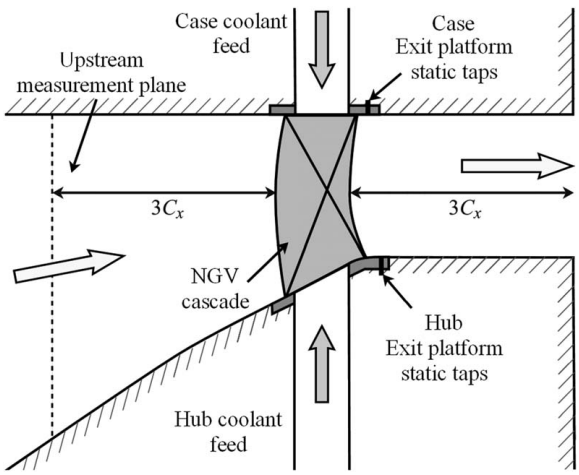

Fig. 1 Simplified diagram of a meridional cross section through the ECAT facility working section

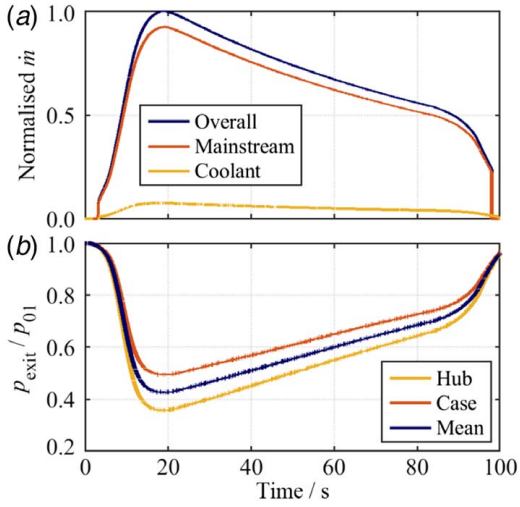

Fig. 2 Trends from a typical experiment of (*a*) mass flowrates and (*b*) vane exit-static to inlet-total pressure ratio

insufficient for the nozzle to choke. The nozzle is then outside of its calibrated range. The data are normalized with respect to the maximum overall mass flowrate. The mass flowrates gradually decay during the test. The coolant-to-mainstream mass flow ratio is held constant during the quasi-steady period ($t = 20$–85 s) at approximately 7.50%.

The facility matches the non-dimensional parameters Mach number, Reynolds number, and coolant-to-mainstream pressure ratio to typical values at engine operating conditions.

Vane inlet total pressure and temperature are each measured at 32 points, distributed circumferentially around the annulus and radially across the vane span, in rakes located three axial chord lengths upstream of the cascade leading edge (see Fig. 1). Vane exit static pressure is measured at 84 tappings located on the hub and case exit platforms of six instrumented vanes distributed around the annulus. The tappings are approximately 5 mm (17% of axial chord length) axially downstream of the midspan TE position. A detailed analysis of these measurements, and their impact on the bias uncertainty in the vane capacity measurement, can be found in Ref. [5]. Vane pressure ratio, p_{exit}/p_{01}, is defined as the ratio of the mean of the 84 exit static pressures to the mean of the 32 inlet total pressure measurements.

During a test, the total pressure and temperature supplied to the test cascade drop as the supply reservoir is depleted. Figure 2(*b*) shows the resulting operating pressure ratio trends across the cascade from a typical test. The mean pressure ratio traverses smoothly through a continuous range $0.42 < p_{exit}/p_{01} < 0.72$ during the quasi-steady period.

The capacity of the fully cooled vane cascade is defined as

$$\Gamma_{vane}\left(\frac{p_{exit}}{p_{01}}, \frac{p_{02}}{p_{01}}\right) = \frac{\dot{m}_1\sqrt{T_{01}}}{p_{01}}\left(\frac{p_{exit}}{p_{01}}, \frac{p_{02}}{p_{01}}\right) + \frac{\dot{m}_2\sqrt{T_{02}}}{p_{02}}\left(\frac{p_{exit}}{p_{01}}, \frac{p_{02}}{p_{01}}\right) + \frac{\dot{m}_3\sqrt{T_{03}}}{p_{03}}\left(\frac{p_{exit}}{p_{01}}, \frac{p_{02}}{p_{01}}\right) \quad (2)$$

where the subscripts 1, 2, and 3 represent mainstream, film cooling (total for all film cooling holes), and TE coolant flows, respectively. Each term is a *surface* of capacity—i.e., a 2D function of the two controlling pressure ratios given in parentheses. This definition allows—in an appropriate experiment—the sensitivity of capacity to changes in individual constituent cooling flows (e.g., TE coolant ejection) to be isolated and examined. It also achieves a level of robustness to changing inlet stream conditions (e.g., T_0) comparable to alternative definitions. The choice of capacity definition is discussed in more detail in Ref. [5]. The three right-hand side terms can be considered as contributions to the overall (or vane)

capacity from each flow. In this case, we take $p_{02} = p_{03}$, since both streams are fed from the same two (hub and case) plena, which are at a common pressure. The capacity definition was consistent between experiments and computational fluid dynamics (CFD).

A capacity *characteristic*—i.e., capacity expressed as a function of the vane pressure ratio, p_{exit}/p_{01}—is generated from a single test. Coolant-to-mainstream pressure ratio, p_{02}/p_{01}, is held at a fixed value. Typically, 20 repeat tests are conducted to reduce the precision uncertainty in the mean capacity measurement. A typical test campaign achieves a precision uncertainty of 0.025% to 95% confidence [5]. Low precision uncertainty is particularly important when considering small capacity changes induced by, for example, a change in TE geometry.

Variation of Trailing Edge Geometry

Four different TE geometries were tested experimentally, with four different SS TE overhang lengths. The four geometries are illustrated in Fig. 3 and are referred to as follows:

Geometry 1: Baseline SS overhang length (approximately 13.4% of the axial chord length)
Geometry 2: Two-thirds of the baseline SS overhang length (approximately 9.0% of the axial chord length)
Geometry 3: One-third of the baseline SS overhang length (approximately 4.5% of the axial chord length)
Geometry 4: No SS overhang (PS and SS TE tips flush in the plane normal to the cascade circumferential direction)—centered-ejection design

NGV capacity is highly sensitive to the precise geometry around the controlling region of the vane passage. As demonstrated previously, a deviation of just 0.1 mm in the passage width close to the plane of minimum physical area, for example, due to a slight shift in the seating of one vane in the cascade relative to its neighbor, would be expected to cause a capacity change of order 1%. Therefore, in order to confidently isolate and assess the impact of varying, for example, TE overhang length, it is critical to ensure geometry remains otherwise identical.

This objective was achieved by generating all four tested TE geometries on the *same set of vane parts*, without disassembling the cascade throughout the duration of testing. The cascade assembly (Fig. 4) was constructed prior to the first set of tests, with the vanes having TE Geometry 1. After the first set of tests, the cascade assembly was removed from the ECAT facility as a single component. At all times when not installed in the facility, a set of five ground steel fixtures each covering 72 deg of the annulus (labeled in Fig. 4) was bolted to the assembly. This ensured that the vanes remained fixed in position throughout the process and prevented stress being imparted to the wet seals. Only one of the five fixtures was removed at any one time to allow the vane TEs located beneath it to be addressed and operated

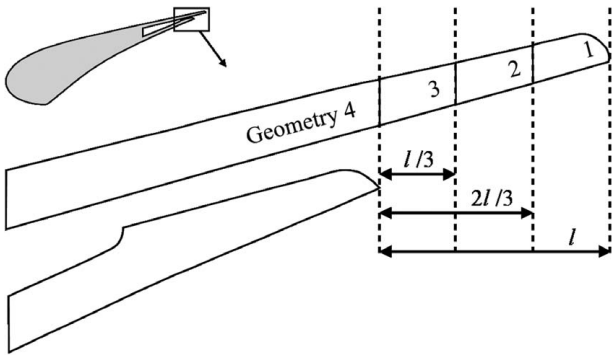

Fig. 3 Diagram showing the four tested TE geometries. The inset in the top-left shows the context of the full vane. *l* is the baseline SS overhang length.

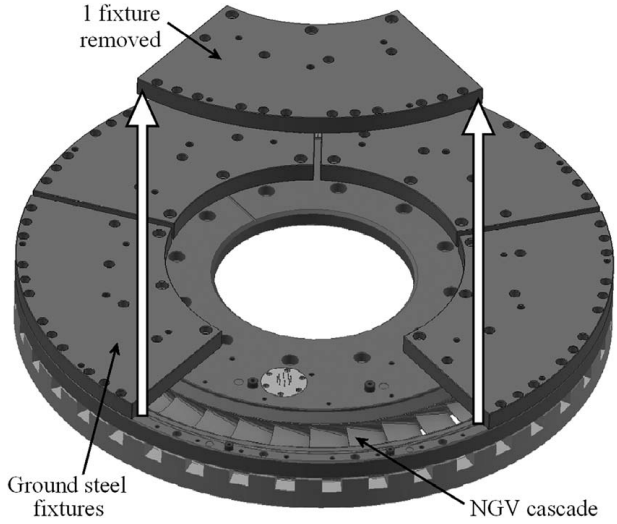

Fig. 4 Diagram of the NGV cascade assembly with ground steel fixtures

on. This is illustrated in Fig. 4. An operation was then performed to cut back the SS TE tip of every vane in the cascade from Geometries 1 to 2 *without* removing any vanes from the assembly. The cascade was then reinstalled in the ECAT facility and tests performed for Geometry 2. This process was repeated to test Geometries 3 and 4 in turn.

The operations performed on the vane TEs are now described. The assembly was placed on a rotating stage on a three-axis computer numerically controlled (CNC) milling machine. The entire assembly could then be finely rotated to accurately address the TE of each vane in turn. For each TE, three separate points along the span were located with an edge-finding tool and compared against a CAD drawing of the nominal part. The nominal TE profile was thus adjusted on a vane-by-vane basis to account for small manufacturing deviations from the nominal geometry. Thus, as far as practically possible, an identical operation was applied to every TE around the annulus. The profile was offset circumferentially by $l/3$ (the increment of material to be removed in each operation—see Fig. 3) to define the path of the cutting tool. The operation was performed using a carbide endmill tool. The NGVs were made of an Inconel alloy with a thermal barrier coating. Care was taken to ensure no debris entered film cooling holes.

The machining process left the SS TE tip in Geometries 2–4 with a squared-off face, as shown in Fig. 3, in contrast to the small radius on the same corner in Geometry 1. The effect of TE shape was examined in detail by Melzer and Pullan [12]. They concluded that the sharp corners of squared-off TEs fix the location of the TE flow separation points, and thus fix the strength of vortex shedding in the transonic regime. This effect can cause squared-off TEs, in some cases, to generate less loss than a rounded TE of equal thickness (when both exhibit transonic vortex shedding). Elliptical TEs were found to suppress transonic vortex shedding, yielding a significant reduction in loss in conditions where it occurs.

The SS TE tip thickness, t, for each geometry is reported in Table 1, normalized with respect to Geometry 1. The thickness of the tip, t, is measured normal to the SS exit metal angle as indicated

Table 1 Passage widths and TE thicknesses for each geometry

Geometry	$w_{PS}/w_{PS,1}$	$w_{SS}/w_{PS,1}$	$w_{SS}/w_{SS,1}$	t/t_1
1	1.000	1.015	1.000	1.000
2	1.000	1.030	1.015	1.085
3	1.000	1.051	1.035	1.204
4	1.000	1.069	1.053	1.310

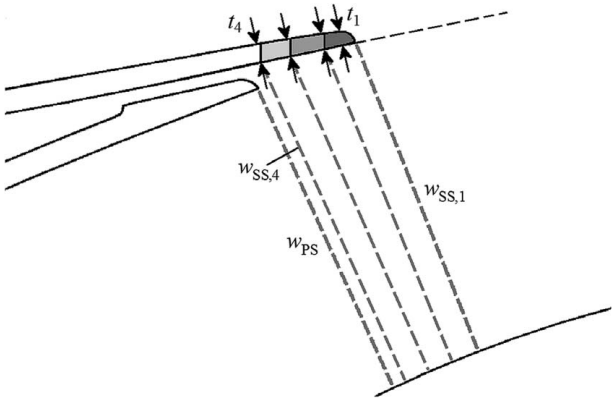

Fig. 5 TE thickness and passage width parameters

in Fig. 5. For Geometry 1, t_1 is measured just upstream of the SS corner radius. Between Geometries 1 and 4, t increases by 31.0%. The minimum physical passage area (marked w_{PS} in Fig. 5) occurs between the PS TE tip and the adjacent vane suction surface. This value is the same for all four geometries. Another measure of passage width is the minimum distance between the SS TE tip and the adjacent vane suction surface (marked w_{SS} in Fig. 5). The values for each geometry, normalized with respect to that for Geometry 1, are reported in Table 1. Between Geometries 1 and 4, w_{SS} increases by 5.3%.

All four TE geometries were tested at the same coolant-to-mainstream total pressure ratio, p_{02}/p_{01}.

Prior to each phase of testing, the coolant capacity characteristic (in the absence of mainstream flow) was measured to ensure that no damage had been sustained to the wet-applied seals. A leak would result in a change in coolant capacity, allowing an imperfect seal to be identified. This method is extremely precise, allowing very small leaks (of order 0.05% of overall capacity at the nominal choked condition) to be detected. The process for measuring the coolant capacity characteristic is described in detail in Ref. [3] (see also Ref. [5]).

Numerical Method

Numerical capacity predictions were made using 3D steady Reynolds-averaged Navier–Stokes (RANS) simulations. The geometry was the rotationally periodic annular sector of two complete NGV passages. This is shown in Fig. 6. The NGV geometry was based on the nominal casting intent (some even more advanced

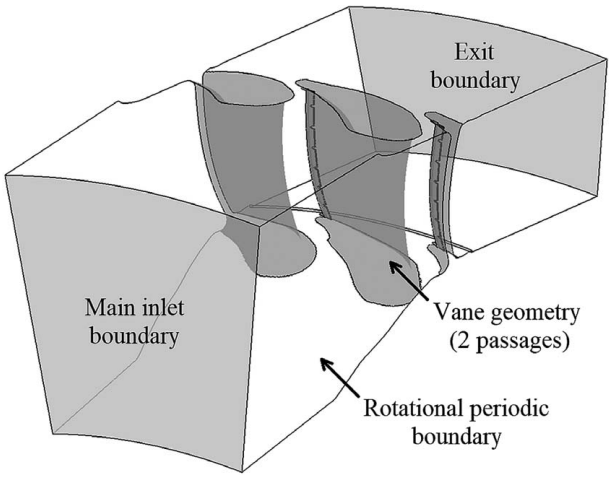

Fig. 6 Geometry for 3D numerical simulations

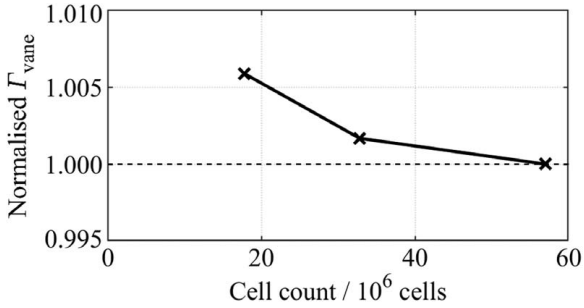

Fig. 7 Normalized vane capacities for CFD solutions with 18 M, 33 M, and 57 M cells

methods use individually scanned parts). The annulus line matches the ECAT facility (see Fig. 1). The TE geometry was modified to match the four tested geometries. *BOXERmesh* was used to generate an octree-based mesh.

A grid independence study was performed with cell counts 18 M, 33 M, and 57 M cells. The predicted capacity values for each grid are summarized in Fig. 7, normalized with respect to the 57 M cell mesh capacity. The change between the 33 M and 53 M cell solutions was 0.17%. The 57 M cell mesh was therefore taken to have sufficiently mesh-independent solutions for comparisons between geometries. Figure 8 shows a midspan section through the mesh for Geometry 1. The left and right edges of the figure are periodic boundaries. The grid was refined around the vane surfaces, in the wake region, and in a region close to the vane TEs. Significant grid refinement was applied across the entire passage width in the controlling region.

A detail of the TE region meshes for all geometries is shown in Fig. 9. Emphasis was placed on minimizing differences in the meshes away from immediate vicinity of the SS of the TE. The value of $y+$ over the PS was in the range 1–5, and over the SS in the range 3–6. Here, we are concerned with aerodynamics and not heat transfer, and these values were considered adequate for the purpose. Uniform inlet conditions of total pressure, total temperature, and turbulence intensity were set on the main inlet boundary plane, matched to the corresponding experimental values. These values are summarized in Table 2. An area-average static pressure condition was specified at the exit boundary, with radial profile arising from radial equilibrium (unconstrained). Extreme care was taken to ensure that the vane pressure ratio condition was defined in the same way in CFD as in the experiment. The CFD mean exit static pressure was taken as the mean of 84 locations matched to the experimental tapping locations, and the CFD inlet total pressure was uniform. A detailed uncertainty study is presented in Ref. [5].

Film cooling flows were modeled using source-terms: mass flowrates and direction vectors were specified on a per-hole basis.

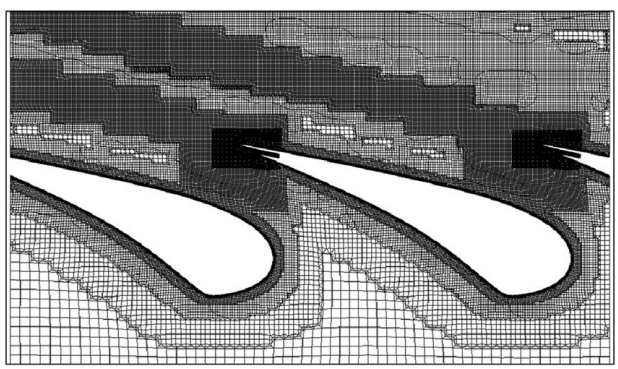

Fig. 8 Midspan section through the mesh for Geometry 1

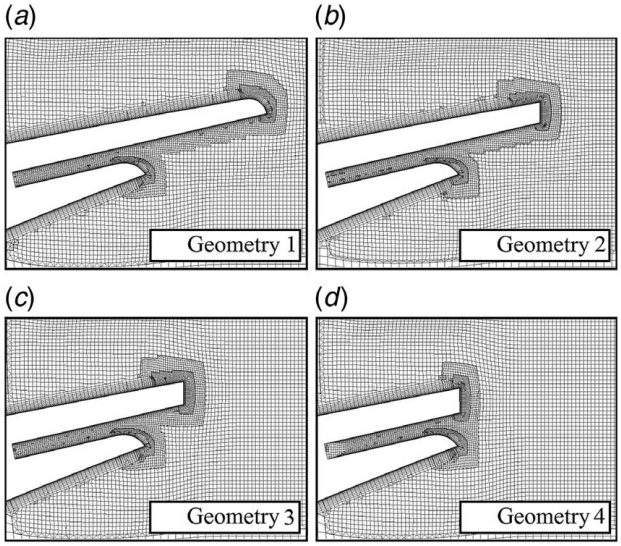

Fig. 9 Detail of midspan sections through TE region meshes

Table 2 Experimental and CFD boundary conditions

Variable	Experiment	CFD
p_{01} (bar)	2.00	2.00
T_{01} (K)	286	286
Tu	~10%	10%
p_{exit}/p_{01}	0.542	0.542
p_{02}/p_{01}	1.025	1.025

The capacity characteristics for individual cooling rows (including the TE slot) were taken from the nominal cooling design for the vane, allowing expected mass flows at experimental conditions (of total pressure and temperature, etc.) to be calculated. *Per-hole* mass flowrates were calculated based on the variation in hole-exit static pressure, evaluated from preliminary uncooled simulations. A common scaling factor (close to unity) was applied to all rows to match the overall coolant stream capacity measured experimentally at the same pressure ratio. Boundary conditions of inlet mass flowrate and total temperature are specified at the TE slot inlet boundaries (total pressure calculated by the solver).

Simulations were performed using a density-based RANS solver in ANSYS CFX with second order discretisation. The shear stress transport (SST) k–ω model was employed for turbulence closure. This is a common choice for studies of this type due to its hybrid nature combining the strengths of standard k–ε and k–ω models which perform well in the freestream and inner regions of the boundary layer, respectively.

A single experimental test produces a capacity characteristic covering a range of pressure ratio, which is compared to the CFD-predicted capacity value at a single vane pressure ratio. The nominal operating point of $p_{exit}/p_{01} = 0.54$ was used for the comparison.

Experimental and Numerical Capacity Characteristics

Experimental measurements and numerical predictions of vane capacity are now presented for TE Geometries 1–4.

Figure 10 compares the measured capacity characteristics (functions of p_{exit}/p_{01}) for all four TE geometries with CFD-predicted results at a single operating point. All data are normalized with respect to the experimental capacity for Geometry 1 at the design pressure ratio ($p_{exit}/p_{01} = 0.542$).

Consider first the experimental characteristic for Geometry 1. In the subsonic range ($p_{exit}/p_{01} > 0.5283$), the capacity characteristic is within $\pm 0.50\%$ of the isentropic trend. The isentropic curve (dashed line) is matched to the experimental measurement for Geometry 1 at the design pressure ratio. As p_{exit}/p_{01} falls below 0.5283, the characteristic increasingly diverges from the isentropic trend. That is, rather than plateauing at the nominal choked condition, the gradient of the curve increases with reducing pressure ratio. At $p_{exit}/p_{01} = 0.46$, the measured capacity is higher than the isentropic value by 1.1%. The flow in the controlling region is complex, featuring TE shocks, unsteady vortex shedding effects, and an interaction between the two wakes (SS and PS *lands* of the vane), the mainstream and the cooling flow. For this reason, there should be no expectation of 1D isentropic behavior.

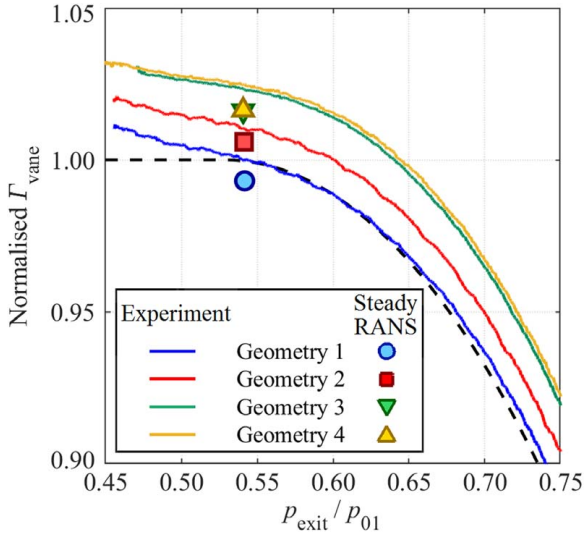

Fig. 10 Experimental capacity characteristics (solid lines) and CFD-predicted capacity (single points) for each TE geometry, normalized with respect to Geometry 1 at the design condition ($p_{exit}/p_{01} = 0.542$)

Comparing the experimental characteristics for Geometries 1–4 in Fig. 10, the trends with changing overhang length are extremely similar. Figure 11 shows the difference between the characteristics as a function of vane pressure ratio. At the design point ($p_{exit}/p_{01} = 0.54$), the differences 1–2, 1–3, and 1–4 are +0.968%, +2.306%, and +2.516%, respectively. As the TE is cut back (i.e., overhang gets shorter), capacity increases monotonically, but with little

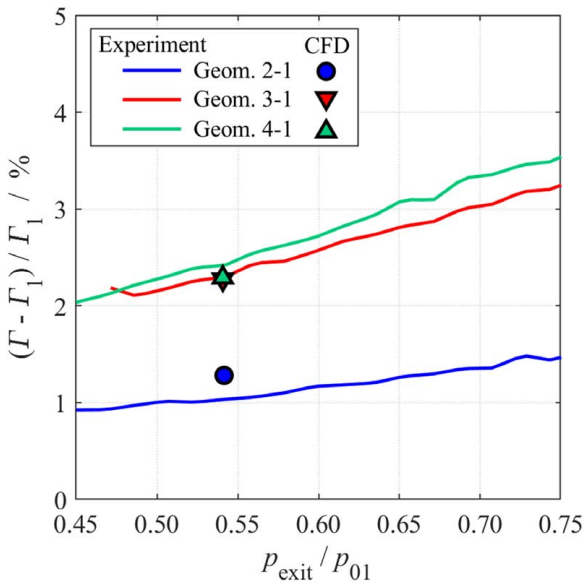

Fig. 11 Percentage capacity changes between Geometries 1–2, 1–3, and 1–4 as functions of vane pressure ratio

Table 3 Summary of percentage capacity changes relative to Geometry 1 from experiment and CFD at $p_{exit}/p_{01} = 0.542$

Geometry	SS overhang length, l	$\Delta\Gamma$ from Geometry 1 (%)	
		Experiment	CFD
1	1.000	–	–
2	0.667	+0.968	+1.298
3	0.333	+2.306	+2.272
4	0.000	+2.516	+2.291

change for the final cutback (moving from Geometry 3 to 4). The mechanisms underlying this will be examined in greater detail later. Looking at the trends with pressure ratio in Fig. 11, the capacity increase (between geometries) with overhang length rises as pressure ratio is reduced. This is a consistent trend for all of the geometries tested.

We see from Fig. 10 that the absolute accuracy of the CFD predictions is extremely good. At the design point, CFD-predicted vane capacity deviated from the absolute experimental capacity measurements by −0.691%, −0.417%, −0.705%, and −0.812% for TE Geometries 1–4, respectively. The average under-prediction was therefore −0.656%. This is well within the typical range of accuracy for well-calibrated numerical methods (indeed ±2% might be considered more typical). Finally, looking at the predictions for the capacity change with overhang length, differences between CFD simulations 1–2, 1–3, and 1–4 are +1.298%, +2.272%, and +2.291%, respectively. These differ in absolute terms from the experimental differences between cases by +0.330%, −0.033%, and −0.225%. This is taken to be extremely good agreement in terms of absolute level of difference.

The experimental and computationally predicted capacity changes are tabulated in Table 3 (for a pressure ratio of $p_{exit}/p_{01} = 0.542$) and plotted in Fig. 12. Overall, the experimental trends seem well behaved, and there is a close match between CFD results and experiment, both in terms of absolute levels and trend with overhang.

Analysis

In this section, we attempt to understand the underlying mechanisms for the change in capacity with changing overhang length. The analysis is progressed under the following five headings:

(1) Analysis of coolant stream capacity changes
(2) Analysis of changes in surface boundary layer profiles due to aerodynamic changes
(3) Simplistic analysis of vane total pressure loss
(4) Incomplete model of the controlling region
(5) Analysis of the aerodynamic flow field in the controlling region

Analysis of Coolant Stream Capacity Changes. In this section, we consider the impact on overall capacity of changes (between geometries) in coolant capacity. This has the potential to affect the overall capacity through changes in the total pressure deficit (or surplus) in the mixing layer [6] on the vane surfaces (which passes through the controlling region of the vane) or through changes in the TE slot flow.

In the experiment, the coolant-to-mainstream total pressure ratio was set to a nominal value of 1.025 with high precision (root-mean-square (RMS) variation of within 0.5% of the coolant-to-mainstream total pressure differential), and the total coolant mass flowrate (sum of film and TE coolant) was measured to precision and bias uncertainties of ±0.08% and ±1.62%, respectively. Thus, the *in situ coolant capacity characteristic* can be accurately determined in each experiment [3,5]. The process for setting the row-by-row mass flowrates in the CFD model has been described,

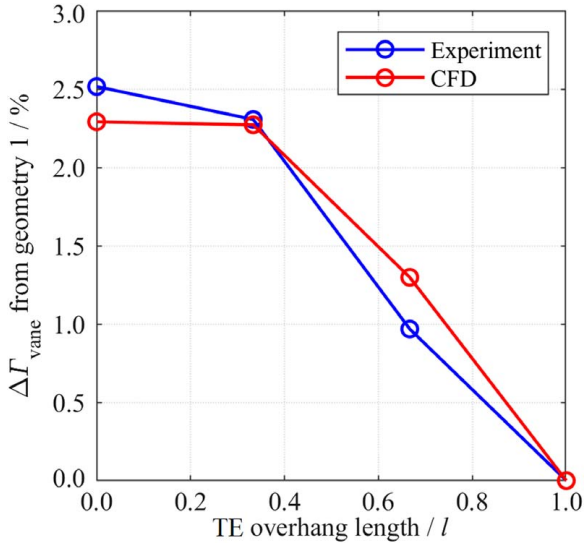

Fig. 12 Change in vane capacity relative to Geometry 1 as a function of TE overhang length for $p_{exit}/p_{01} = 0.542$

and these are accurately matched to the experimental condition at the relevant pressure ratio.

To understand the impact on overall capacity of changes in film cooling and TE slot flows, it is necessary first to deconstruct the in situ cooling capacity characteristic into film and TE slot flow characteristics. These two flows were not independently measured in the experiment, and the method of deconstruction, while accurate, is somewhat involved. The method is described in detail in Appendix A. We now consider the impact of changes in film and TE capacity in turn.

We find that the largest inferred (from measurement) change in *film* capacity between any two TE geometries (Geometries 1–4) was +0.18% of Γ_{vane}. Using a method developed by Povey [8], we estimate the resultant impact on overall capacity as a reduction of −0.005% of Γ_{vane} (i.e., the loss developed in the mixing layer outweighs the effect of enhanced total pressure at the ejection point). This is negligible in comparison to the observed changes in overall capacity, and we therefore conclude that the effects due to changes in film cooling flows alone are relatively insignificant.

The largest inferred (from measurement) change in TE coolant capacity between geometries (Geometries 1–4) was +0.037% of Γ_{vane}. Although we will later show that there is a moderate change in base pressure between geometries, the fact that the TE slot flow operates at large overall pressure ratio means that the impact of base pressure changes on the TE flow capacity is relatively small. In a later section, we present models of interaction between mainstream and TE slot flows with different TE overhang lengths. It is argued that there is some interaction between these flows that is model-dependent (and, therefore, geometry-dependent), but always with an *exchange rate* between TE slot flow and overall flow in the range 0–1 (see the models in Fig. 13 and the associated arguments). That is, the absolute maximum overall capacity change that might be expected from the model would be +0.037% of Γ_{vane}. This is more than an order of magnitude smaller than the measured overall vane capacity change. We conclude that the change in TE slot capacity is not, in isolation, responsible for the observed vane capacity change with changing overhang length.

In summary, we conclude that neither the changes in film cooling nor TE coolant flows are significant contributors to the observed changes in vane capacity between TE geometries.

Analysis of Changes in Surface Boundary Layer Profiles Due to Aerodynamic Changes. This section considers how aerodynamic changes arising from changes in TE geometry impact the boundary layer profiles in the controlling region of the passage,

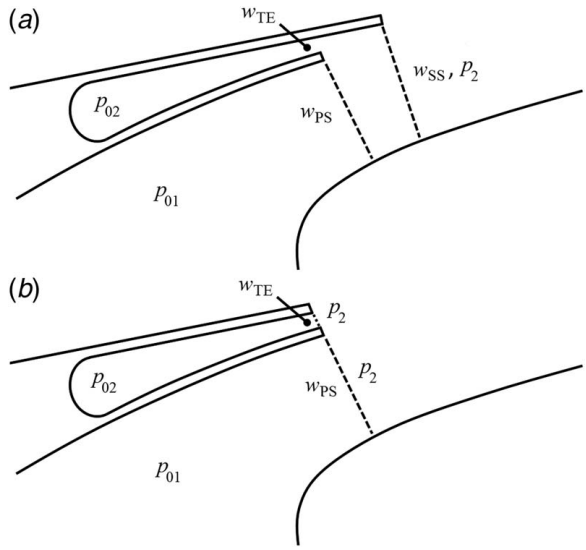

Fig. 13 Schematic diagrams representing model (*a*), a model with common controlling area, model (*b*), a model with independent controlling areas

and consequently the overall capacity. The fundamental mechanism is that mass flow *deficit* within the boundary layer—measured, e.g., with respect to the ideal, inviscid (non-zero slip at the wall) case—reduces the passage mass flowrate. This can be represented by the displacement thickness, δ^*. Changes in δ^* between geometries would affect the overall capacity. This analysis is related to that of Fielding [2,13], in that it considers the capacity change due to effective blockage caused by passage frictional losses.

Boundary layer velocity profiles predicted by CFD at both the SS and PS limits of the plane of minimum physical area (w_{PS}) at midspan are presented in Appendix B for all four TE geometries. Displacement thicknesses, δ^*, and corresponding passage mass flow deficits (estimated as $\dot{m} = \rho U \delta^* h$, where ρ and U are the flow density and velocity at the boundary layer edge and h is the vane span) were evaluated for each profile and summarized in Table 6 in Appendix B.

For each of Geometries 2–4, there was a small (of order −10%) reduction in boundary layer displacement thickness with respect to Geometry 1 and a corresponding negligible rise (of order +0.04%) in passage mass flowrate. These changes are an order of magnitude smaller than the observed capacity changes. We therefore conclude that the difference in passage mass flowrate between geometries arising due to changes in boundary layer velocity deficit cannot alone be a significant mechanism responsible for the observed changes in measured vane capacity.

Simplistic Analysis of Vane Total Pressure Loss. In this section, we consider the impact on overall capacity of changes (between geometries) in the row efficiency or total pressure loss, of the vane, due to aerodynamic changes caused by changes in TE geometry.

So far as capacity is concerned, a typical NGV is a fundamentally 2D (or higher, if radial pressure gradients are considered) system. The sonic line is often far from aligned with the plane of minimum area for example and instead crosses obliquely. One-dimensional analogies are therefore at best incomplete and at worst highly misleading. By this, we mean that the 1D model in which the vane is represented by a unique area (or *throat*), with associated upstream total pressure and temperature conditions, and a corresponding downstream static pressure, is not an adequate description of the system. The problem of reducing our particular system to a 1D system can be illustrated with reference to Fig. 5. Here, as we change from Geometry 1 to Geometry 4, the area w_{PS} is fixed while w_{SS} changes. The entire flow also passes through a common downstream area (e.g., a fixed area axial plane) but at an angle which has a complex dependence on the vane aerodynamics. This determines the *true area* in the streamwise direction. The distributions of total pressure, Mach number, and flow angle have complex relationships with each other and differ between the four geometries. The concept of a unique area for our 1D model is thus problematic.

Notwithstanding this rather fundamental problem, it is worth noting that there were some serious early attempts to develop models based on 1D analogies. To the extent that these partially capture the true overall system, they can be considered useful. One such model is that of Fielding [2,13] who, in what might be considered a quasi-2D framework, defined a *restriction factor*, which described the degree to which passage frictional losses reduced the nozzle effective flow area with respect to the ideal, frictionless case. This model accounted for the fact that the loss was concentrated within the boundary layers, not distributed uniformly across the passage.

In Appendix C, we explore the extent to which a relatively simple quasi-2D analysis of this type can provide any insight into our system. We adapt the Fielding [2] model (consideration of total pressure loss) to include information about passage area for our particular system, in an attempt to predict capacity changes with TE geometry changes. A somewhat arbitrary choice must be made about the definition of total pressure loss, and with this choice comes an associated definition of passage area. We argue the case for representing total pressure loss using downstream total pressure characteristics (experimental traverse measurements or CFD-predicted distributions) and passage area with a new concept that we refer to as a *repeating area unit*. The repeating area unit is a physical area in the guided part of the vane, aligned as normal as possible to the assumed flow direction. It is chosen to provide the most direct possible analogy to a 1D system, which is necessary for the quasi-2D approach that is developed. The arguments around these choices are elaborated in Appendix C. We use the adapted model to attempt to reproduce the experimentally measured and CFD-predicted changes in vane capacity.

We conclude (see Fig. 27 in Appendix C) that a simple area-loss model in the spirit of Fielding [2] does not meaningfully reproduce the observed capacity changes between all geometries. For small changes in overhang length, the model performance was reasonably good: the modeled capacity change for Geometry change 1–2 agreed to within 0.32% of Γ_{vane} for experiment and to within 0.20% of Γ_{vane} for CFD. Good agreement was expected because the primary changes in the flow field could be approximated by a 1D model. The model performance was poor for Geometry change 1–3 and very poor for Geometry change 1–4. In the latter case, the model over-predicted the changes in experimentally measured and CFD-predicted capacities by 2.71% and 3.79% of Γ_{vane}, respectively. The poor agreement was to some extent expected due to the more significant (2D) aerodynamic changes which cannot be represented within the framework of the quasi-2D model.

The conclusion is that simple area-loss models of this kind are inadequate for analyzing even relatively small capacity changes when there is any significant change in the 2D aerodynamics.

Incomplete Models of the Controlling Region. In this section, the flow field through the controlling region of the vane passage is examined more holistically in an attempt to explain the observed changes in vane capacity.

We first introduce two *incomplete* models of the vane passage. By incomplete we mean that while the models convey one important interactive effect in the flow (between the TE slot flow and the mainstream) they do not, in isolation, explain the capacity trends observed in experiments when TE overhang length is reduced. The two models (a) and (b) are represented in Fig. 13. In these models, the mainstream and TE flows have uniform total pressures p_{01} and p_{02}, respectively, and exhaust to a common static pressure p_2.

In model (a), the two *controlling areas* w_{PS} and w_{TE} (for the mainstream and TE flows, respectively) pass through a common third

controlling area, w_{SS}, which marks the exit static pressure boundary for the system. In this model, the three controlling areas are highly interacting, as the TE slot mass flow (and associated total pressure profile, including loss from separation off the SS overhang) partially mixes with the mainstream flow before passing through the controlling area w_{SS}. The interaction is complex, but we highlight one important aspect of the dynamics. For fixed w_{PS} and w_{TE}, and fixed p_2 at the controlling area w_{SS}, the static pressure achieved at the exits w_{PS} and w_{TE} is affected by the area-ratios w_{PS}/w_{SS} and w_{TE}/w_{SS}. That is, if the TE overhang length is changed such that w_{SS} changes, the static pressures and mass flowrates at exits w_{PS} and w_{TE} would also be expected to change. Thus, we would expect small changes in overhang length (and w_{SS}) to affect the overall system mass flowrate and hence capacity.

With reference to Fig. 5, it is possible to argue that model (a) is relevant to the incremental changes between Geometries 1 and 2 and between Geometries 2 and 3, but less relevant to the change between Geometries 3 and 4. Examining the TE geometries, we find that $w_{SS} < (w_{PS} + w_{TE})$ for Geometries 1 and 2, but $w_{SS} > (w_{PS} + w_{TE})$ for Geometries 3 and 4. That is, the minimum area, in this simplified model, switches from the downstream area w_{SS} to the combination of the individual areas $w_{PS} + w_{TE}$ between Geometries 2 and 3. The model would seem to go some way to explaining the observed capacity changes between Geometries 1–2 and 2–3. The mechanism underlying this in the model is the reducing back-pressure at w_{PS} and w_{TE} as w_{SS} is increased, for the same pressure p_2 at w_{SS} (within the framework of the model).

In model (b), the TE overhang is entirely removed so that the PS and SS lands are flush. Here, there are effectively two *independent controlling areas*, w_{PS} and w_{TE}, for the mainstream and TE flows, which exhaust to a common exit static pressure. The absence of the third controlling area w_{SS} reduces the complexity of the interplay between the mass flowrates associated with w_{PS} and w_{TE}. In this model, small changes in overhang length are not expected to significantly affect the overall system capacity characteristic, in line with the very small capacity change between Geometries 3 and 4 (Fig. 10), in a region in which $w_{SS} > w_{PS} + w_{TE}$.

We have already noted that these models are incomplete, but they do provide some insight into one important mechanism. We have used the term *controlling area* to describe a *series* of interacting areas. Even in these simplistic and incomplete models (Fig. 13), the controlling areas are identified to be somewhat arbitrary (identified only as easily identifiable and measurable minima) planes within a looser *controlling region*. We explicitly distinguish these concepts from well-defined *throats* (with their associated and extremely unhelpful connotations of 1D flow) because of the fundamental 2D nature of the pressure field in typical vane passages.

While their simplicity makes 1D analogies attractive, in a typical vane passage, the pressure contours pass through the point of minimum area at a high angle (often up to 45 deg). This alone is sufficient to demonstrate the weakness of the 1D analogy. To conclude, none of the controlling areas *choke* in a conventional sense, and it would be hard to say that any one were more important than any other. It is the *general* pressure field developed in the controlling region (i.e., the loosely defined transonic region around the vane minimum area) that is responsible for setting vane capacity.

Analysis of the Aerodynamic Flow Field in the Controlling Region. In this section, changes in the aerodynamic flow field as the TE overhang length is reduced are analyzed.

Figures 14(*a*)–14(*d*) show CFD-predicted contours of midspan Mach number for Geometries 1–4, respectively, at a nominal pressure ratio $p_{exit}/p_{01} = 0.54$. The pressure ratio was defined as described in the earlier sections. The locations of planes w_{PS} and w_{SS} are marked.

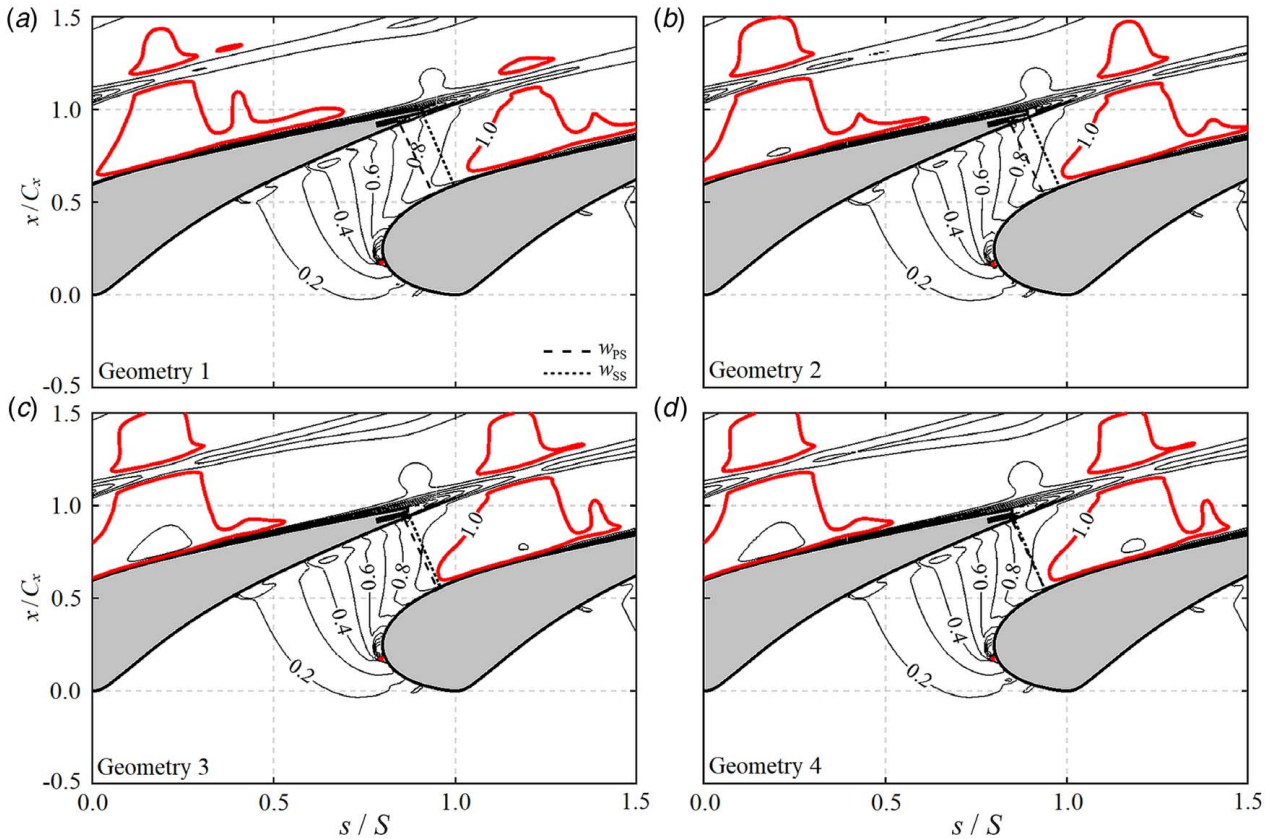

Fig. 14 Contours of Mach number in a section through the controlling region of the vane passage at the midspan radius for each TE geometry. $M = 1.0$ contour is marked in bold. The locations of the w_{PS} and w_{SS} areas are indicated by dashed lines.

For all geometries, the contours of Mach number cross the midspan w_{PS} line at roughly 45 deg. This is due to the combined effect of streamwise acceleration and turning. The pressure field is strongly 2D, evidenced by the acute angle between Mach contours and the local flow direction, even for the moderately forward loaded vanes used in this study. For Geometry 1, the Mach number distribution along the line w_{PS} is from around 0.7 near the PS to 0.9 near the SS. The $M = 1.0$ contour (bold line in Fig. 14) lies wholly downstream of the plane w_{PS}.

As the TE overhang is reduced, moving from Geometries 1 to 3, three main effects occur: (i) the M contours gradually migrate upstream, leading to higher velocities at the plane w_{PS}; (ii) the mildly supersonic region on the late SS deepens, broadens, and penetrates through the wake region into the neighboring passage flow; and (iii) the wake region deepens and broadens, indicating increased total pressure loss. Between Geometries 3 and 4, changes in the flow field are almost negligible. These effects are in line with the observed changes in capacity with changing TE overhang length (Figs. 11 and 12) and—to the extent they are valid—with the models represented in Fig. 13.

The same trends can be observed by examining the isentropic Mach number distributions for each geometry, which are shown in Fig. 15. The abscissa for each curve is the axial distance normalized by the axial chord *for that specific geometry*. The location of the intersection on the vane SS of the plane w_{PS} is marked with a black circle for each geometry. This occurs at approximately 55% axial chord. Isentropic Mach number is normalized with respect to the mean exit Mach number for Geometry 1. The overall distributions are characteristic of a moderately forward loaded NGV. Apparent discontinuities in the profile are associated with local accelerations and diffusions around cooling holes. When presented in this way, the PS distributions for all geometries are extremely similar up to around 0.9 C_x. Acceleration continues up until the PS TE lip, which occurs at progressively later fractions of axial chord as the TE overhang is reduced (moving from Geometry 1 to Geometry 3). The peak Mach number at the TE lip increases incrementally between Geometries 1 and 3 as the M contours shift upstream (Fig. 14). Peak Mach numbers on the PS TE lip for Geometries 1–4 were 0.81, 0.92, 0.97, and 0.98, respectively.

Reducing TE overhang length leads to increased mid-to-late SS acceleration, with the most significant changes occurring around the *controlling region* of the passage, close to the intersection of w_{PS} with the vane SS. The peak Mach numbers achieved on the SS were 1.08, 1.10, 1.12, and 1.13 for Geometries 1 to 4, respectively, in agreement with the loading redistribution (Fig. 14).

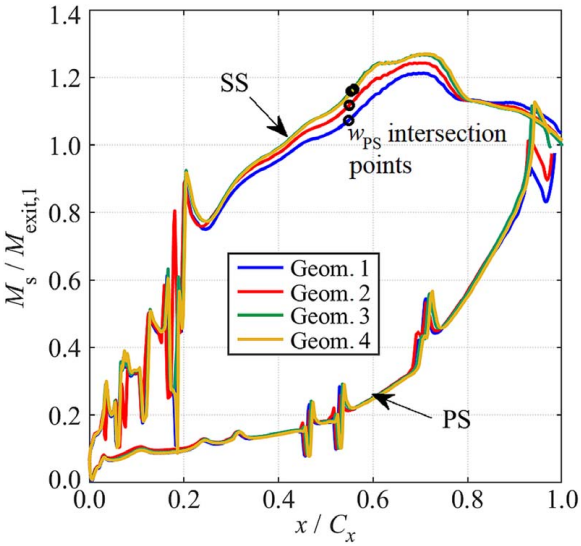

Fig. 15 Normalized vane surface isentropic Mach number distributions at midspan for each TE geometry

Mach number and total pressure distributions across the planes w_{PS} and w_{SS} are now examined. Figure 16 shows contours of Mach number on the planes w_{PS} and w_{SS} for each TE geometry. Axes correspond to normalized distance across the passage from PS to SS (x-axis) and normalized span (y-axis). Corresponding normalized total pressure distributions are presented in Fig. 17. Profiles along the midspan line (span fraction 0.5) are extracted and plotted in Fig. 18. Looking first at Mach number (Fig. 16), the following observations are made:

(i) The Mach distribution at plane w_{PS} is primarily 2D (streamwise and cross-passage) in nature, for all four geometries. This means that most of the behavior can be explained by examining 2D trends.
(ii) The distribution of M at plane w_{SS} is more 3D in nature (increased radial variation, especially between 0% and 25% span) than at w_{PS}. The radial variation is reduced for very short TE overhang length (Geometry 4).
(iii) The distribution of M at plane w_{SS} is less sensitive to TE overhang length than that at plane w_{PS}, particularly for Geometry changes 1–2 and 2–3. Recall from Fig. 14 that the M contours migrate gradually upstream, but note that plane w_{SS} also moves upstream somewhat in-step with the M contours, in contrast to plane w_{PS} which is fixed in place. The M distribution at plane w_{SS} is a greater function of the exit boundary condition and overall vane aerodynamics than that at plane w_{PS}, which additionally depends on the interaction between the mainstream and TE flows, and the two planes (see models of Fig. 13).
(iv) The low M region at the PS extremes of the w_{SS} planes, associated with the TE flow and the PS side of the wake region, deepens and broadens as TE overhang is reduced. This arises as the w_{SS} plane moves gradually closer to the PS TE and so less mixing has taken place between the mainstream and TE flows.

Notwithstanding the low M region associated with the TE flow and wake in the w_{SS} distributions, the M contours are very similar between w_{SS} and w_{PS} for Geometry 4, but quite different for Geometry 1. This is to be expected for two reasons: first, the two planes move gradually closer in space as we move incrementally from Geometry 1 to Geometry 4 (see Fig. 5); second, the interactive effect of the two controlling areas becomes less significant both as their values become closer in magnitude and also as the flow system transitions towards one in which two flows (mainstream and TE) pass through a common area (model (a) in Fig. 13) as opposed to two separate areas (model (b)).

Consider now the normalized total pressure distributions in Fig. 17. We observe the following:

(i) The distribution of normalized total pressure is essentially 2D in nature, for all geometries and in both planes. The behavior can be explained accurately by examining 2D trends.
(ii) Normalized total pressure is very uniform and approximately equal to unity over the central region of the passage (20–80% of passage width). Loss in this region is minimal, arising only from turbulent dissipation, so this result is expected.
(iii) There are reduced total pressure regions near to both the PS and SS surfaces, associated with film cooling flows. The total pressure deficit is greater on the SS (as expected for mixing at higher average freestream Mach number) and the mixing layer is thinner (as expected for the strongly accelerated, and therefore thinning, SS boundary layer).

The only significant difference between the total pressure profiles at w_{SS} and w_{PS} is due to the additional deficit associated with the wake from the PS TE and the relatively low-momentum TE slot flow. As in the M distributions, the low total pressure region changes in profile with TE overhang length. In Geometry 4, as w_{SS} and w_{PS} are very close, the region of pressure deficit is

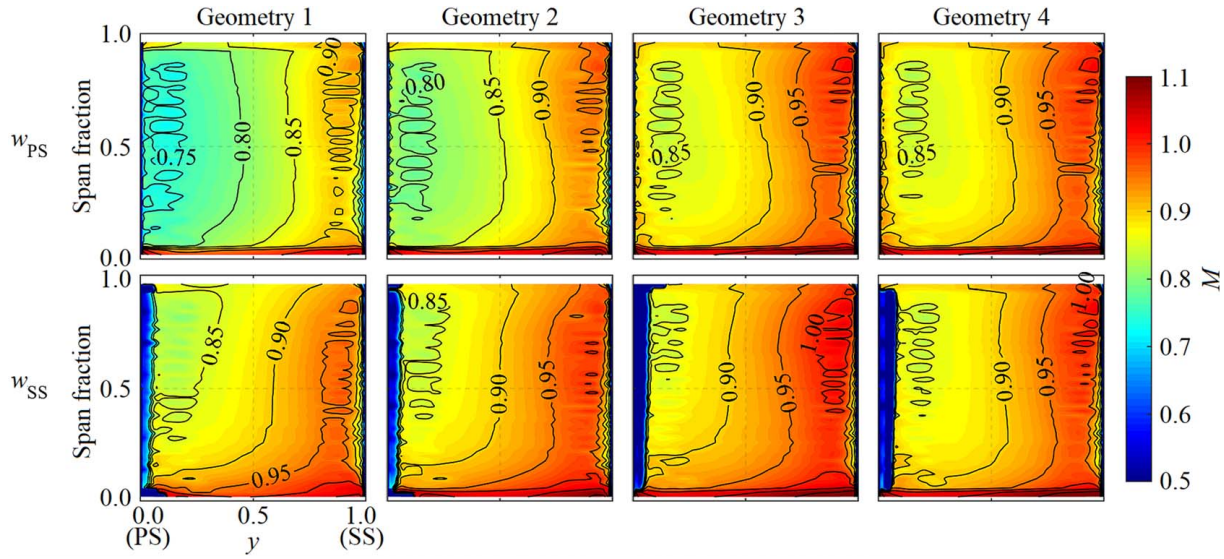

Fig. 16 Contours of Mach number in planes w_{PS} and w_{SS} for each TE geometry

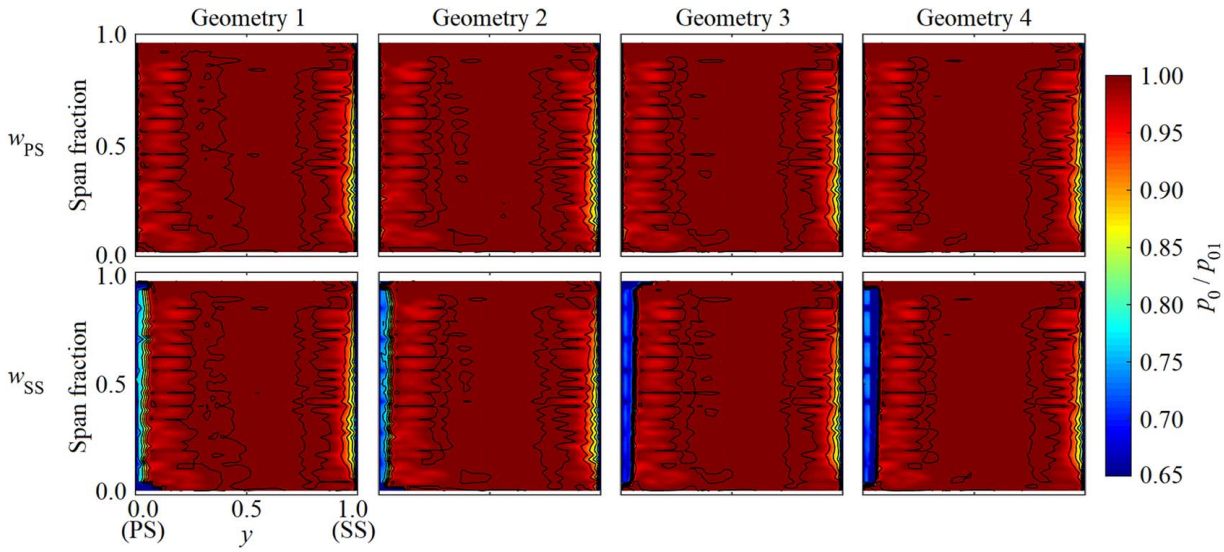

Fig. 17 Contours of normalized total pressure in planes w_{PS} and w_{SS} for each TE geometry

essentially unmixed and manifests as a thicker, more sharply defined layer than for Geometry 1, for which mixing has attenuated the depth of the low total pressure region.

Figure 18 presents midspan data (averaged over 45–55% of vane span) for all TE geometries at planes w_{PS} and w_{SS}. Subplots (a)–(f) show normalized total and static pressure, Mach number, whirl angle, deviation angle, and normalized mass flowrate, respectively. Schematic diagrams of the passage explaining the controlling area nomenclature, and angle definitions, are presented in (g) and (h), respectively. The plots of physical parameters are now analyzed in turn.

Figure 18(*a*) complements the normalized total pressure distributions in Fig. 17. For all geometries, total pressure is essentially equal to the inlet condition between 20% and 80% passage width at both w_{PS} and w_{SS}. As TE overhang is reduced (moving from Geometries 1 to 4), the high loss region on the extreme PS of the passage (0–8% passage width) deepens and the transition to the central region becomes much steeper as the plane w_{SS} approaches w_{PS}. There are very small changes in both the boundary layer and coolant mixing losses associated with aerodynamic changes for the vane.

Figure 18(*b*) shows static pressure profiles at midspan. All geometries and both planes exhibit a similar cross-passage pressure gradient, the result of the potential field effect due to upstream covered turning and downstream uncovered turning. At planes w_{SS}, the change in static pressure field between geometries is relatively small. We infer that for all geometries, the aerodynamic relationship (remaining turning, TE loss, mixing of adjacent streams, etc.) between the controlling area pressure distribution and the downstream pressure distribution (which was fixed in all cases) is similar.

In contrast, at plane w_{PS}, the static pressure is much higher than at plane w_{SS} for Geometry 1. This results from the competing controlling areas shown in model (a) in Fig. 13. As the TE overhang is reduced, the static pressure at plane w_{PS} continually decreases until, for Geometry 3, the difference from that at plane w_{SS} is very small. There is no further change in static pressure between Geometries 3 and 4. This is in accord with model (b) of Fig. 13. The average static pressure differences between planes w_{PS} and w_{SS} were 10.6%, 7.5%, 1.3%, and 1.2% of $p_{01} - p_{exit}$ for Geometries 1–4, respectively.

Figure 18(*c*) more clearly exemplifies the conclusions regarding the *M* distributions of Fig. 16. The *M* distributions (*c*) closely follow

the static pressure distributions (*b*), due to the almost matched total pressures (*a*). In plane w_{SS}, the distribution changes little as TE overhang is reduced—the only significant change is in the separated region of the PS land wake and the low-momentum TE slot flow. The shift between Geometries 1 and 4 to a sharper drop in M occurs as plane w_{SS} moves closer to w_{PS}, leading to a less mixed out profile in the plane w_{SS}. In contrast, there is a significant change in M at plane w_{PS}. The trends at plane w_{PS} share a similar shape but are incrementally offset between the geometries, with peak values 0.91, 0.94, 0.98, and 0.98 for Geometries 1–4, respectively. The magnitudes of these increments are in line with the observed capacity trends (Figs. 11 and 12); the observed upstream shift in M contours with respect to the fixed w_{PS} plane between Geometries 1 and 3 but not 3 and 4 (Fig. 14) and also with the analysis presented in the context of Fig. 13. This indicates significant interaction between the areas w_{PS} and w_{SS} for Geometry changes 1–2 and 2–3 (model (a)) and low interaction for Geometry change 3–4 (model (b)). The magnitudes of the increments are also in line with the static pressure variation in Fig. 18(*b*), the total pressure profiles (Fig. 18(*a*)) being similar for all geometries.

Whirl angle, β, is plotted in Fig. 18(*d*). β is defined as the angle between the local velocity vector, v, and the axial direction, $\hat{n}_x$, as shown in Fig. 18(*h*). For controlling area $w_{SS,1}$, the associated unit normal vector, $\hat{n}_{SS,1}$, and the angle $\theta_{SS,1}$ between $\hat{n}_{SS,1}$ and $\hat{n}_x$ are also marked. θ angles for each plane are listed in Fig. 18(*i*). Similar definitions apply for other planes. In both the planes w_{PS} and w_{SS}, the whirl angle variation across the passage is relatively small, falling by approximately 2–3 deg between 20% and 80% of passage width moving from PS to SS.

Looking first at planes w_{SS}, whirl angle drops significantly as TE overhang length is reduced. The average changes between 20% and 80% passage width were −1.50 deg, −1.51 deg, and −0.69 deg for Geometry changes 1–2, 2–3, and 3–4, respectively. Unlike other variables, while the change between Geometries 3 and 4 is lower than those seen for the other changes, it is not negligible. This is expected both because the *covered turning length* is reduced and because the angle of the local surface tangent on the SS limit of the w_{SS} planes is also reduced with each incremental geometry change. Planes w_{PS} have much less sensitivity to the geometry changes. The average changes in whirl angle between 20% and 80% passage width were −0.33 deg, −0.37 deg, and −0.05 deg for Geometry changes 1–2, 2–3, and 3–4, respectively. The geometry upstream of w_{PS} is unchanged, but the flow still responds to static pressure changes (potential field effect) caused by the reduced covered turning downstream of the w_{PS} plane.

It is interesting to consider an effective *deviation angle*, $\delta = \beta - \theta$, with respect to the individual controlling planes. Deviation angle is plotted in Fig. 18(*e*). Positive deviation angles represent overturning with respect to a specific controlling area, and vice-versa. On the SS of the passage, deviation angles are close to zero. Here the flow follows the SS surface angle, and any deviation from zero (neglecting small boundary layer displacement effects, etc.) arises from the controlling area-normal direction ($\hat{n}_{SS,1}$, $\hat{n}_{SS,2}, \ldots, \hat{n}_{PS}$) not being precisely aligned with the local SS surface tangent. Towards the PS of the passage, deviation angles are positive. The gross trend results from the average metal angle at the PS limit of the planes w_{SS} and w_{PS} being greater than θ (the PS limit is at full-chord, while the SS limit is around half-chord, with remaining turning downstream).

An indication of the mass flow deficit that could be attributed to unaligned flow (angular difference between v and $\hat{n}$ at a particular plane) can be obtained by finding the average value of the cosine of δ over the 20–80% of passage width. For the planes w_{SS}, we get 0.0070%, 0.0004%, 0.0004%, and 0.0057% for Geometries

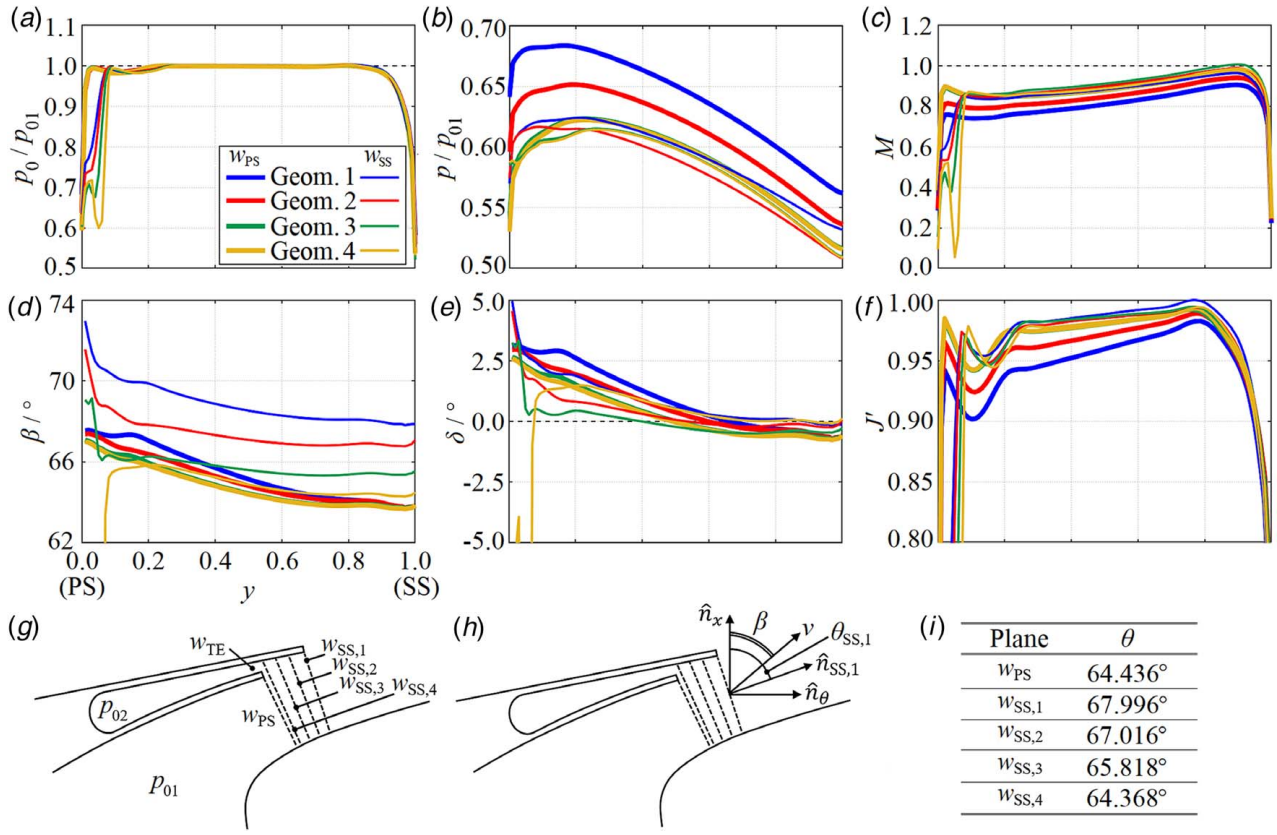

Plane	θ
w_{PS}	64.436°
$w_{SS,1}$	67.996°
$w_{SS,2}$	67.016°
$w_{SS,3}$	65.818°
$w_{SS,4}$	64.368°

Fig. 18 Midspan profiles in planes w_{PS} and w_{SS} of (*a*) normalized total pressure, (*b*) normalized static pressure, (*c*) Mach number, (*d*) whirl angle, (*e*) deviation angle, (*f*) normalized local capacity, and schematics of (*g*) controlling areas, (*h*) angle definitions, and (*i*) summary of area-normal angles, θ

1–4, respectively. The corresponding values for planes w_{PS} are 0.0110%, 0.0042%, 0.0004%, and 0.0002%. These values are very small and show that while there are measurable changes in deviation between the geometries, this effect is not particularly significant in the context of the measured capacity changes.

Finally, we evaluate the local mass flowrates per unit area, normalized with respect to upstream total conditions (p_{01}, T_{01}) for each geometry. This can be considered a local capacity function. The maximum local mass flux occurs for Geometry 1 in plane $w_{SS,1}$. A *dimensionless local capacity* can therefore be defined as

$$J' = \frac{\left[(\delta\dot{m}/\delta A)\sqrt{T_{01}}/p_{01}\right]_{\text{local}}}{\left[(\delta\dot{m}/\delta A)\sqrt{T_{01}}/p_{01}\right]_{\text{SS,1,max}}} \tag{3}$$

where δA is a local area element, and $\delta\dot{m}$ is the associated element of mass flowrate. Profiles of J' for each geometry are plotted in Fig. 18(*f*). As expected, the profiles have significant local mass flow deficits near the PS ($y<0.2$) and SS ($y>0.8$) limits, caused by boundary layer loss and total pressure deficit due to coolant-mainstream mixing. In the near-PS flow, the coolant and boundary layer losses are distinct whereas in the near-SS flow, the two effects merge into a single deficit region. The general trend is towards lower J' on the lower Mach number PS of the passage (the flow being essentially subsonic).

We now consider changes in J' distribution across the passage as TE overhang length is reduced. *Changes in* J' with respect to Geometry 1 for each of Geometries 2–4 are shown in Fig. 19.

At the planes w_{SS}, the changes in J' between geometries are small and negative over most of the passage. In the relatively *clean* (i.e., unaffected by mixing interactions with boundary layers, cooling flows, or TE slot) flow region ($0.2<y<0.8$), the average changes in J' were −0.365%, −0.216%, and −0.594% for the Geometry changes 1–2, 1–3, and 1–4, respectively. The changes in w_{SS} between geometries, expressed as a percentage, and the changes in $\overline{\Delta J'}$ between geometries, expressed as a percentage, are listed in Table 4. An estimate of the capacity changes expected on the basis of area and aerodynamic changes in the clean flow region (due to the gross potential field) can be found by calculating the changes in the product of J' and w_{SS}. The changes in the product for each geometry change, expressed as a percentage, are listed in Table 4.

Comparing this with the CFD-predicted overall capacity changes (Table 3, reproduced in Table 4 for convenience), we see that this estimation is in good agreement for Geometry change 1–2, but overestimates the capacity changes for Geometry changes 1–3 and 1–4.

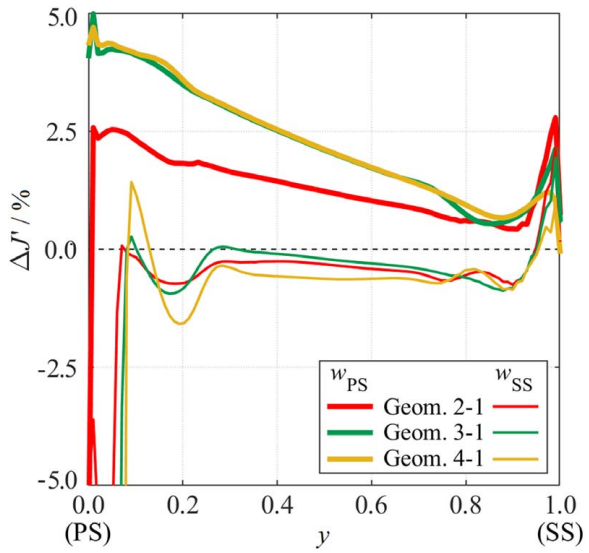

Fig. 19 Change in non-dimensional local capacity, J', as a function of cross-passage location for each geometry

Table 4 Summary of changes in passage width and average $\Delta J'$ between geometries for planes w_{SS} compared to CFD-predicted capacity changes

Geometry change	Δw_{SS} (%)	$\overline{\Delta J'}$ (%) ($0.2<y<0.8$)	$\Delta(w_{SS}\times\overline{J'})$ (%)	$\Delta\Gamma$ (%)
1–2	+1.534	−0.365	+1.116	+1.298
1–3	+3.522	−0.216	+3.241	+2.272
1–4	+5.290	−0.594	+4.587	+2.291

Table 5 Summary of changes in average $\Delta J'$ between geometries for planes w_{PS} compared to CFD-predicted capacity changes

Geometry change	$\overline{\Delta J'}$ ($0.2<y<0.8$) (%)	$\Delta\Gamma$ (%)
1–2	+1.204	+1.298
1–3	+2.078	+2.272
1–4	+2.087	+2.291

The deterioration in the accuracy of the estimation arises because there are changes in the mixing region between the TE flow and the mainstream (as the overhang length becomes short and the dynamics of the controlling region change as proposed in Fig. 13) which are not included in the assessment of the change in J'.

Performing the same analysis for planes w_{PS}, we see that changes in J' with geometry variation are significant, with large increments of change between Geometries 1–2 and 2–3, but almost no further change between Geometries 3–4. This trend is consistent with the observed overall capacity trend and the models (a) and (b) of Fig. 13. Changes in J' are greatest on the PS of the passage, where the flow is well below peak capacity (see Fig. 18(*c*)). Near the PS ($y\approx0.05$), the Mach numbers were 0.75, 0.81, 0.87, and 0.88 for Geometries 1 to 4, respectively. Near the SS ($y\approx0.90$), the higher Mach numbers (0.90, 0.94, 0.98, and 0.98) limit the potential field-induced changes in J' between geometries, due to the lower gradient of the capacity characteristic. The average changes in J' over $0.05\le y\le0.90$ (taken as the region unaffected by near-wall effects and hence $\Delta J'$ is due only to gross potential field effects) were 1.20%, 2.08%, and 2.09% for Geometry changes 1–2, 1–3, and 1–4, respectively. These values are listed in Table 5 and compared with the CFD-predicted capacity changes (from Table 3). The area w_{PS} is fixed between all geometries, the boundary layer effect has been established to be small, and the complex interactions associated with the mixing TE flow are far less significant than at plane w_{SS}. Good agreement is therefore expected between $\overline{\Delta J'}$ and $\Delta\Gamma$. From Table 5, we see that $\overline{\Delta J'}$ and $\Delta\Gamma$ agree to within 0.2% of absolute capacity, or, on average, to within 8.2% of the registered change.

We conclude by comparing the streamlines through a midspan section between Geometries 1 and 3. These are shown in Fig. 20. Streamlines originating from the TE coolant ejection slot are marked in bold.

Mainstream flow on the vane PS flows over the PS TE tip and turns into the PS base region (point 1 in Fig. 20(*a*)), where it meets coolant flow ejected from the TE slot. With a relatively long TE overhang (e.g., Geometry 1), the inner surface of the SS TE provides further turning—of the mixing TE coolant and PS mainstream flow—away from the axial direction. When the mixing PS mainstream and TE flows reach the SS TE tip, they then turn into the SS base region (point 2 in Fig. 20(*a*)). They meet with the SS mainstream flow at the so-called *point of confluence* (point 3 in Fig. 20(*a*)) and are turned to a common exit flow angle. This determines the location of the wake region with respect to the vane geometry.

As TE overhang length is reduced, the inside surface of the SS TE has less impact on the path of the mixing PS mainstream and TE flows. They therefore turn into the SS base region further

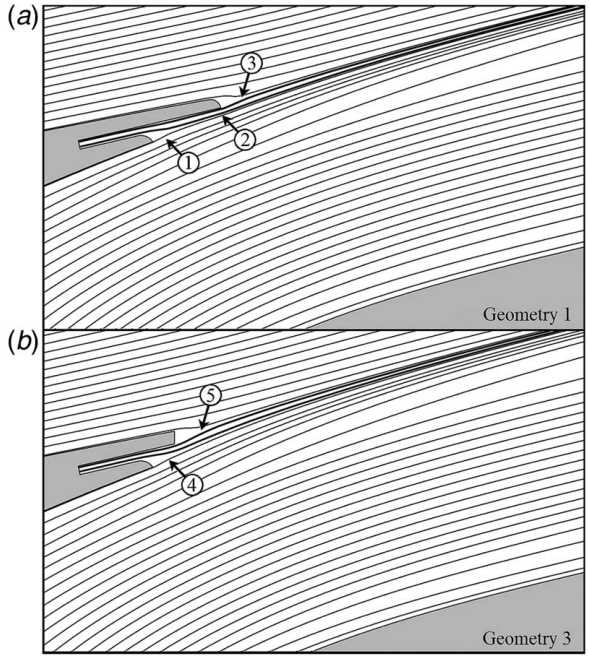

Fig. 20 Streamlines in a midspan section for (*a*) Geometry 1 and (*b*) Geometry 3

upstream (e.g., point 4 in Fig. 20(*b*)). The location of the point of confluence between mainstream flows from the PS and SS also moves circumferentially upstream (compare the location of point 5 in Fig. 20(*b*) relative to the PS TE tip with that of point 3 in Fig. 20(*a*)). The effect of this is to slightly shift the path of the wake with respect to the vanes.

When TE overhang becomes short (Fig. 20(*b*)), the PS and SS TE tips form a combined base region and the path of the mixing PS mainstream and coolant flows is not significantly affected by the short remaining SS overhang. Further reductions in overhang length (e.g., moving from Geometry 3 to 4) therefore have almost no impact on the streamlines, and the locations of the point of confluence and the wake region remain the same.

Summary and Conclusions

The impact of TE overhang length on capacity has been evaluated using both ultra-low uncertainty experimental methods and numerical methods. A parametric set of four different TE designs was investigated, providing an opportunity to understand the absolute and relative accuracies of the CFD method for this environment, the sensitivity to geometry changes of this type, and the fundamental mechanisms for capacity change. The conclusions in each of these areas were as follows:

Absolute and relative accuracies of CFD method: CFD capacity predictions agreed with experimental measurements to within −0.691%, −0.417%, −0.705%, and −0.812% for TE Geometries 1–4, respectively. The RMS error was 0.672%. The absolute accuracy of the CFD method was therefore extremely good. The *relative* accuracy of the CFD (in terms of the *changes* in capacity with changing TE overhang length) was good, matching observed experimental changes to within +0.330%, −0.033%, and −0.225% for respective changes of magnitude +1.298%, +2.272%, and +2.291%. The CFD method was therefore validated for aiding in the understanding of the underlying mechanisms responsible for the observed capacity changes.

Geometry sensitivity: A monotonic increase in vane capacity was observed as TE overhang length was reduced. The percentage capacity increases relative to Geometry 1 measured in experiments were +0.968%, +2.306%, and +2.516% for Geometries 2–4, respectively (nominally equal changes in overhang length). The gradient of the capacity trend reduced greatly when overhang length became small, partly explained by a change in the way the controlling areas interact.

Fundamental mechanisms for capacity change: Detailed analysis was conducted into the fundamental mechanisms responsible for the observed capacity shift between geometries and potential models through which the system behavior could be understood. This analysis was split into five areas, drawing the following conclusions:

(1) *Coolant stream capacity changes*: Neither changes in film cooling flows nor TE coolant flows between TE geometries were found to be significant in relation to the changes in vane capacity.
(2) *Changes in surface boundary layer profiles*: Analysis of the vane surface boundary layer displacement thicknesses and associated mass flow deficits showed that while there are small differences between the geometries, they are an order of magnitude smaller than the measured capacity changes. It was therefore concluded that this is not a significant mechanism responsible for the vane capacity shift.
(3) *Simplistic total pressure loss model*: A simple model of the vane was developed which included a total pressure loss model related to that of Fielding [2] and a *repeating area unit* to represent changes in area. A typical NGV is a fundamentally 2D system (sonic line far from aligned with the minimum area plane). The intrinsically 1D notion of a *throat* therefore provides a wholly inadequate description of the system. Even thinking of a *particular* controlling area is misleading and problematic, due to the necessary arbitrariness with which it must be ascribed in systems of this type. A more complete model of the vane should include *several* interacting controlling areas or a more general *controlling region*. This terminology is considered important as it sets the framework for thinking about the problem. Notwithstanding these deficiencies, the simple model performed moderately well for very small geometry changes (Geometries 1–2) when applied to both experimental and CFD data. For more significant geometric changes, the model significantly over-predicted the capacity change and could in no way predict the change in behavior once overhang length became small. We conclude that fundamentally 1D area-loss models cannot adequately represent the response of the physical system to even small aerodynamic changes and are therefore too simplistic to be useful.
(4) *Models of the controlling region*: Two more complex models of the vane were introduced, tailored to the two extremes of the TE geometry variation. The first model had a shared controlling area through which passed two interacting flows (and a wake). The second model had two non-interacting, independent controlling areas. While these models were incomplete, they represented an important aspect of the changing flow interactions between TE geometries that was necessary to progress more detailed analysis. The switch-over between the two models can be predicted by inspection of the controlling areas for each geometry.
(5) *Aerodynamic flow field changes*: The complex changes in the flow field between geometries have been understood by examining in detail the full-area and midspan 2D profiles of total and static pressure, Mach number, whirl angle, and local specific capacity, focusing on changes in the controlling region (considered in the framework of the two models proposed in this paper). The flow was primarily 2D in nature and well described by considering midspan trends (but with a radial pressure field superimposed). Total pressure profiles through the controlling region were similar between all geometries, as were static pressure distributions when examined at a downstream controlling area (w_{SS} planes), confirming a similar aerodynamic relationship between the pressure distributions at the controlling area and the far downstream system boundary.

Static pressure distributions at an upstream controlling area (w_{PS} planes) were much more sensitive to TE geometry, due to a complex interaction in the controlling region, analyzed as an interaction between two controlling areas. These changes were the primary driver for significant changes in the Mach number and associated local specific capacity distributions at the w_{PS} planes. When analyzed at the w_{PS} planes, the combination of changes in area and local specific capacity closely reconcile the measured vane capacity changes for all TE geometries. This was not true for w_{SS} planes. This difference in behavior is attributed to the w_{SS} planes being affected by the separation downstream of the PS TE tip, something not included in the model.

In summary, we conclude that although the capacity changes between geometries *can* be explained using a model which includes the area and static pressure changes at a particular controlling area, the model is somewhat system-dependent, and a more complete description is provided by holistically analyzing the aerodynamic change in the entire controlling region. Low-order system representations of the type proposed in this paper are tempting because of the conceptual simplification they offer, but, we feel, are ultimately inadequate as descriptions of the system.

Acknowledgment

The support of Rolls-Royce plc is gratefully acknowledged, as is the contribution of Dominic Harris to the operation of the experimental facility.

Nomenclature

h = vane span, m
k = arbitrary constant
l = baseline PS TE overhang length, m
p = static pressure, Pa
s = circumferential distance, m
t = SS TE thickness, m
u = velocity, m s^{-1}
w = passage width associated with "repeating area unit" of vane passage, m
x = axial distance, m
y = wall-normal distance or normalized distance across passage, m
A = area, m^2
J = local capacity function, s K$^{1/2}$ m^{-1}
M = Mach number
S = vane pitch, m
U = velocity at edge of the boundary layer, m s^{-1}
Tu = turbulence intensity
$\dot{m}$ = mass flowrate, kg s^{-1}
$\dot{m}_{TOT}$ = total (mainstream + coolant) mass flowrate, kg s^{-1}
$\hat{n}$ = unit vector
J' = non-dimensional local capacity ratio
p_0 = stagnation pressure, Pa
p_{exit} = mean vane exit static pressure, Pa
w_{PS} = passage width in the plane of the PS TE tip, m
w_{SS} = passage width in the plane of the SS TE tip, m
w_{TE} = TE slot thickness, m
$y+$ = non-dimensional wall distance
C_x = axial chord length, m
M_{exit} = mean vane exit Mach number
M_s = isentropic Mach number
T_0 = stagnation temperature, K
Y_p = profile stagnation pressure loss coefficient

Greek Symbols

β = flow turning (or whirl) angle
Γ = capacity, m s K$^{1/2}$
Γ_i = isentropic capacity, m s K$^{1/2}$
Γ_{vane} = vane (or overall) capacity, m s K$^{1/2}$
δ = deviation angle
δ^* = boundary layer displacement thickness, m
θ = plane-normal angle
ρ = mass density, kg m^{-3}
φ = restriction factor (defined in Ref. [2])

Subscripts

0 = stagnation conditions
1 = mainstream vane inlet condition or TE Geometry 1
2 = film coolant inlet condition
3 = TE coolant inlet condition

Appendix A: Changes in Vane Capacity Due to Changes in Coolant Stream Capacities

Figures 21(*a*) and 21(*b*) show the mainstream and coolant capacity terms (deconstructed from the results presented in Fig. 10) for both experiment and CFD. At the design point, the total cooling flow (films and TE slot) makes up approximately 8% of the overall (mainstream and coolant) flow.

In Fig. 21(*b*), the overall cooling flow is further deconstructed into film cooling and TE slot flow characteristics. These two flows are not independently measured in the experiment, and the deconstruction is performed via a model. The model uses a series of CFD runs—performed at a range of off-design vane pressure ratios—to determine transfer functions between the vane pressure ratio and the individual film-row pressure ratios. The capacity characteristic for each row (including the TE slot) was assumed to have the isentropic form *when presented in terms of the local exit-static-to-inlet-total pressure ratio*. The ratio of magnitudes of the individual row characteristics came from the cooling design analysis for the engine part. The individual row characteristics were then expressed in terms of the vane pressure ratio using the transfer functions, and the total coolant capacity characteristic—as a function of p_{exit}/p_{01}—was determined by summing the individual row characteristics. The row characteristics were then scaled by a constant, $c = f(p_{exit}/p_{01})$, so that the model-predicted total coolant capacity characteristic matched the experimentally measured value for each vane pressure ratio. This method preserves the relative gradients of the individual coolant capacity characteristics and is believed to perform this deconstruction accurately.

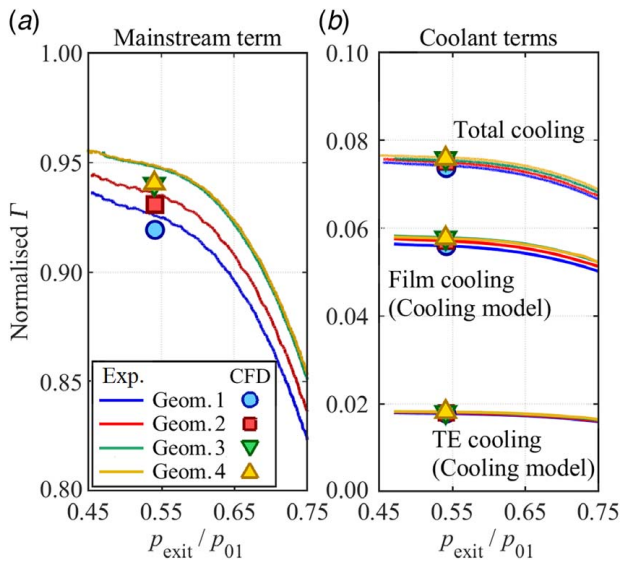

Fig. 21 Mainstream (*a*) and coolant (*b*) capacity terms for each TE geometry, normalized with respect to the experimental overall capacity for Geometry 1 at the design pressure ratio

Consider first the *experimentally measured* total coolant capacity characteristics. From an absolute level of 7.4% of the total (mainstream plus cooling) capacity, the experimental changes between Geometries 1–2, 1–3, and 1–4 represented as *percentages of overall cooling flow* were +1.01%, +1.66%, and +2.42%, respectively. Expressed as *percentages of total capacity*, the corresponding numbers were approximately +0.08%, +0.12%, and +0.18%. These are very small changes, and not—in isolation—expected to significantly alter the state of the boundary layer flow passing through the controlling region. The film cooling model of Povey [6] estimated an exchange rate between film cooling mass flow (or capacity) and overall mass flow (or capacity) of −0.0269 at typical cold test rig conditions. Taking the largest change of +0.18% (between Geometries 1 and 4), this would lead to a predicted *decrease* in overall vane capacity of −0.0049%. The conclusion is that the effect of film cooling on boundary layer loss is entirely negligible in comparison to the observed change in overall capacity between Geometries 1 and 4 (+2.5%; see Table 3) and can be ignored.

We turn now to the TE coolant flow. Using the model-based deconstruction into film cooling and TE slot flows, it is predicted that approximately 85.8% of the mass flow increase (for all cases) is due to film cooling, with the remaining 14.2% due to the TE slot. Expressed as a percentage of total capacity, the predicted (model-based) changes in TE slot flow between Geometries 1−2, 1−3, and 1−4 are +0.014%, +0.031%, and +0.037%, respectively. These are very small changes in comparison to the observed change in overall capacity between Geometries 1 and 4 (+2.5%; see Table 3). It is worth noting that the TE slot flow is less sensitive both to local aerodynamic changes (the split we are currently discussing, at a fixed vane pressure ratio) and global aerodynamic changes (Fig. 21(*b*) shows lower gradient of capacity with p_{exit}/p_{01} for TE slot compared to film cooling rows) because it operated at a much higher overall pressure ratio than the (capacity) average overall pressure ratio of the film cooling rows.

Appendix B: Changes in Passage Mass Flow Deficit Due to Changes in Surface Boundary Layer Profiles

CFD-predicted boundary layer velocity profiles at the plane of minimum physical area (w_{PS}) at midspan are plotted in Fig. 22 for each of the four TE geometries. Both PS and SS profiles are plotted. Velocities are normalized with respect to the local free-stream velocity, U. In the case of the PS boundary layer, there is a fairly strong velocity gradient in the wall-normal direction, y, and therefore the value at a local peak (at a normalized passage width of approximately 0.018) is taken. The SS layer has a gradual velocity variation in the wall-normal direction, which makes the value of U rather arbitrary. For the purpose of plotting, U is defined as the velocity at a normalized wall-normal distance of $y/w_{PS} = 0.03$. Both surface profiles are characteristic of fully turbulent flow. This is expected at these locations (near PS TE and just over 50% of axial chord from the SS leading edge) for a fully cooled HP NGV.

Because of the difficulty in defining the outer edge of the boundary layer, the displacement thickness, δ^*, is computed for each of the eight boundary layer profiles for all integral heights between the wall ($y/w_{PS} = 0$) and $y/w_{PS} = 0.04$. The variation of normalized displacement thickness, δ^*/w_{PS}, with integration height is shown in Fig. 23. For a boundary layer with zero wall-normal velocity gradient, an asymptotic approach to a well-defined value of δ^* would be expected. In this case, because of the strong wall-normal velocity gradient over length scales comparable to the displacement thickness, the value of δ^* is poorly defined. The profiles of δ^*/w_{PS} as a function of integration height, y/w_{PS}, do plateau, however, allowing a displacement thickness to be estimated. Here we refer to the volume flow deficit caused both by shear with the wall and mixing in the film cooling layer. With reference to Fig. 23, the PS and SS integrals are seen to plateau for integration ranges of around $0 \le y/w_{PS} \le 0.015$ and $0 \le y/w_{PS} \le 0.030$, respectively. These limits are marked in the figure.

The values of δ^*/w_{PS} returned for these integration ranges are summarized in Table 6. Corresponding mass flowrate deficits are estimated as $\Delta\dot{m} = \rho U \delta^* h$, where h is the vane span. Here we make the approximation that δ^* is broadly uniform over the vane span. These deficits and the *changes* in mass flowrate deficit with respect to Geometry 1 are also tabulated in Table 6. In the final column, negative values indicate a *reduction* in mass flow *deficit* due to a thinner boundary layer region—i.e., a rise in overall passage mass flowrate. We see from Table 6 that, while there are small differences between the four geometry cases, these differences are an order of magnitude smaller than the observed capacity changes (see Table 3 and Fig. 12).

Appendix C: Application of the Simplistic Area-Total Pressure Loss Model

In an earlier section of this paper, the quasi-2D model of Fielding [2,13] was introduced. In this model, a *restriction factor* is defined as a way of describing the reduction in nozzle effective flow area

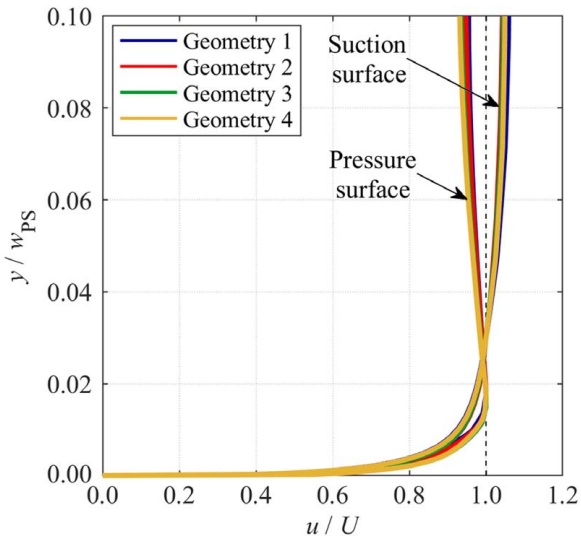

Fig. 22 Normalized PS and SS boundary layer velocity profiles in the w_{PS} plane at midspan for each TE geometry

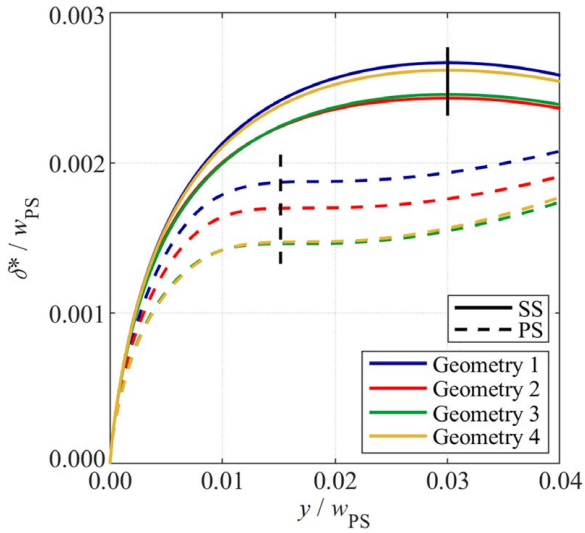

Fig. 23 SS and PS boundary layer displacement thicknesses as functions of wall-normal integration height, y, for each TE geometry

Table 6 Estimated boundary layer displacement thickness, overall mass flowrate deficit, and change in mass flow deficit relative to Geometry 1

Geometry	PS $\delta^*/w_{PS} \times 10^{-3}$	SS $\delta^*/w_{PS} \times 10^{-3}$	SS + PS $\Delta\dot{m}/\dot{m}_{TOT}$(%)	SS + PS $\Delta\dot{m}/\dot{m}_{TOT}$ (related to Geometry 1)
1	1.88	2.67	0.403	–
2	1.70	2.43	0.372	−0.035%
3	1.47	2.46	0.358	−0.040%
4	1.48	2.62	0.374	−0.022%

due to frictional effects within the passage. The loss correlations of Ainley and Mathieson [14] and Dunham and Came [15] were used to estimate the boundary layer thickness integral parameters. For an exit Mach number $M_{exit} > 0.8$, the restriction factor φ resulting from the analysis was well approximated by the following simplified form:

$$\varphi = 1 - 0.56Y_p \tag{A1}$$

where the profile total pressure loss coefficient, Y_p, is defined as

$$Y_p = \frac{p_{01} - p_{02}}{p_{02} - p_{exit}} \tag{A2}$$

where p_{exit} is the area-mean static pressure in the traverse plane, p_{02} is the local total pressure in the traverse plane, and p_{01} is the vane inlet total pressure. This may be regarded as a quasi-2D approach, in that the vane model is that of a 1D system (single area, upstream total, and downstream static pressure) but with a loss correction model with a 2D component (distribution of loss across the passage). Loss confined to boundary layer regions has a lesser impact on capacity than uniformly distributed loss. This is represented in Eq. (A1) by the factor of 0.56 being less than unity. The restriction factor provides an estimate of the ratio of actual flow capacity to the 1D isentropic capacity, i.e., $\varphi = \Gamma/\Gamma_i$, where Γ_i is the isentropic capacity characteristic.

We now examine the extent to which this relatively simple quasi-2D analysis, combined with a measure of the change in passage area between different TE geometries, can reconcile the observed results. This requires that somewhat arbitrary choices be made about how the system is represented in terms of both total pressure and area. These choices are now considered in turn.

Because TE loss is an important aspect of the system, near-plane traverse data ($0.50C_x$ downstream of the TE) were chosen as a proxy for total and static pressure through *controlling regions* of the vane. In practice, this is the closest plane in which the entire vane loss, including TE loss, can be evaluated and gives the simplest representation of the back-pressure condition.

Turning to area, we choose a quasi-periodic *repeating area unit* (i.e., including all streamlines exactly once, when *repeated* through the system), related as closely as possible to a physical area in the guided part of the vane and aligned as normal as possible to the assumed flow direction. The purpose is to provide the most direct analogy possible to a 1D system. Noting the rather fundamental weakness in the 1D analogy, the repeating area units are taken as those lines represented by $w_1 = w_{SS,1} + t_1$, $w_2 = w_{SS,2} + t_2$, etc., with reference to Fig. 5. Figure 24 shows a schematic of the repeating area unit so formed. The repeating area unit is not strictly periodic due to the difference in SS boundary layer state between the two ends of the line w (between mid-chord and the TE). Table 7 summarizes the widths associated with each repeating area unit.

To calculate Y_p, experimental traverse measurements were conducted in an axial plane $0.50C_x$ downstream of the vane TE plane (five-hole pressure probe with tip diameter 2.80 mm), at a nominal pressure ratio $p_{exit}/p_{01} = 0.54$ or $M_{exit} = 0.975$. The downstream area was surveyed over 2.5 vane pitches. The loss characteristic was primarily 2D in nature and is well represented by the circumferential profiles of Y_p at midspan, shown in Fig. 25. The

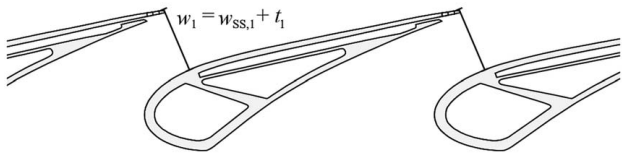

Fig. 24 Schematic diagram of the *repeating area unit*

Table 7 Summary of widths associated with repeating area units for each geometry

Geometry	1	2	3	4
w/w_1	1.000	1.018	1.042	1.064

characteristics have the classic quasi-normal distribution expected for a partially mixed out wake. Moving from Geometry 1 to 4 (reducing TE overhang length), the peak broadens and shifts to a lower value of s/S.

A comparison to CFD-evaluated midspan loss is also shown in Fig. 25. The prediction shows higher peak values of Y_p (wake center) when compared with experiments. This is in line with the well-known tendency of most CFD methods to under-predict the wake mixing rate. Moving from Geometry 1 to 4 (reducing TE overhang length), the change in the CFD-predicted trends agrees with experiment, with a broadening peak moving to lower values of s/S.

To evaluate an average total pressure loss coefficient, $\overline{Y_p}$, the circumferential profiles of local Y_p were mass flow-averaged over two vane pitches (centered on mid-passage to avoid sensitivities). Experimental and CFD averages are plotted in Fig. 26 as functions of TE overhang length, expressed as percentage changes with respect to the longest TE overhang (Geometry 1). The experimental

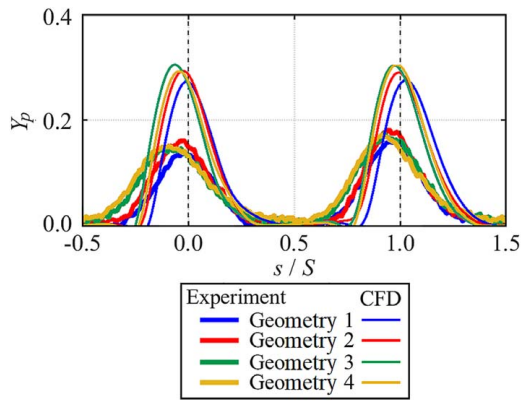

Fig. 25 Experimentally measured and CFD-predicted circumferential profiles of local total pressure loss coefficient, at midspan, $0.50C_x$ downstream of the TE

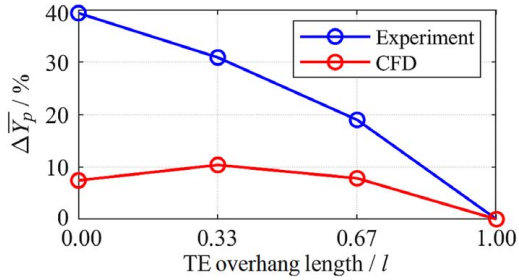

Fig. 26 Percentage change in circumferentially averaged Y_p with respect to Geometry 1 as a function of TE overhang length

Table 8 Summary of average total pressure loss coefficients

	$\Delta\overline{Y_p}$ from Geometry 1 (%)	
Geometry	Experiment	CFD
2	+18.99	+7.82
3	+30.91	+10.38
4	+39.39	+7.41

average value increases monotonically as TE overhang is reduced, up to a 39.4% increase between Geometries 1 and 4. This result is intuitively expected (complexities of interaction with the TE slot flow aside) as the TE becomes less aerodynamic with reducing overhang.

CFD over-predicts the average loss coefficient by an average of 31.9% (across all designs). Moving from Geometry 1 to 3, the predicted trend is similar to experiments, with increasing Y_p as TE overhang length is reduced. The predicted change between Geometries 3 and 4 differs from experiments, with CFD showing a small reduction in Y_p. Percentage changes in average Y_p relative to Geometry 1 are summarized in Table 8 for each of Geometries 2 to 4.

Following the Fielding [2, 13] analysis presented above, the simplest possible capacity model could be regarded as

$$\Gamma \propto w\frac{\Gamma}{\Gamma_i} = w(1 - k\overline{Y_p}) \tag{A3}$$

where k is a constant and w is the width of the repeating area unit (see Fig. 24 and associated discussion). For typical loss distributions across the passage, Fielding [2] determined a value $k = 0.56$. The limiting value for uniformly distributed loss (yielding the smallest capacity change that could be predicted by this model for a given $\overline{Y_p}$) would be $k = 1.00$. We consider both of these values in our modeling to show the typical or extreme minimum capacity changes expected on the basis of this model.

Considering only the *changes* in capacity with TE overhang length (the absolute accuracy of the CFD has been discussed in the context of Figs. 10 and 11), from Eq. (A3), the expected capacity ratio between, e.g., Geometries 1 and 2 could be written as

$$\frac{\Gamma_2}{\Gamma_1} = \frac{w_2(1 - k\overline{Y_{p,2}})}{w_1(1 - k\overline{Y_{p,1}})} \tag{A4}$$

and similarly for ratios Γ_3/Γ_1 and Γ_4/Γ_1.

The model-predicted capacity changes with varying overhang length are now evaluated based on both CFD and experimental $\overline{Y_p}$ data. The predicted changes are compared with the corresponding experimentally measured and CFD-predicted changes. The data are tabulated in Table 9 and are plotted in Fig. 27, in terms of the percentage changes from Geometry 1, i.e., for example,

$$\Delta\Gamma_{1-2}\ (\%) = 100\left(\frac{\Gamma_2}{\Gamma_1} - 1\right) \tag{A5}$$

Data are presented for both $k = 0.56$ and $k = 1.00$. Looking first at the data for $k = 0.56$ (part (a) of Table 9), we see that the model performs reasonably well for small changes in overhang length (Geometry change 1–2), over-predicting the vane capacity change by only +0.323% and +0.197% for experiment and CFD, respectively. The agreement is worse for Geometry change 1–3 (over-predictions of +0.956% and +1.511% for experiment and CFD, respectively) and the performance becomes very poor for the largest change in overhang length (Geometry change 1–4), where the capacity changes are over-predicted by +2.714% and +3.790% for experiment and CFD, respectively.

The same data are plotted in Fig. 27, where capacity changes predicted by the quasi-2D model are plotted against those determined by CFD and experiment. Experimental and CFD points are represented by hollow circles and triangles, respectively. Points lying close to a line of unit gradient (dotted line) indicate accurate prediction. The model clearly shows increasing deviation from ideal prediction as the geometry change becomes more significant (1–3 and 1–4). The loss-based model is therefore a very poor predictor of capacity change.

We now consider data for $k = 1.00$ (part (b) of Table 9). This value maximizes the sensitivity of the capacity change to changes in measured total pressure loss. Due to the increasing total pressure loss with each successive geometry change (see Tables 8 and 9), increasing k has the effect of reducing the predicted increments of

Table 9 Summary of changes in vane capacity with respect to Geometry 1 predicted by the simple area-loss model applied to both experimental and CFD loss data for values (a) $k = 0.56$ and (b) $k = 1.00$

		Experiment				CFD			
Geometry change	$\frac{w}{w_1}$	$\frac{\overline{Y_p}}{\overline{Y_{p1}}}$	$\frac{(\Gamma/\Gamma_i)}{(\Gamma/\Gamma_i)_1}$	$\Delta\Gamma_{model}$ (%)	$\Delta\Gamma_{meas.}$ (%)	$\frac{\overline{Y_p}}{\overline{Y_{p1}}}$	$\frac{(\Gamma/\Gamma_i)}{(\Gamma/\Gamma_i)_1}$	$\Delta\Gamma_{model}$ (%)	$\Delta\Gamma_{pred.}$ (%)
(a) $k = 0.56$									
1–2	1.018	1.190	0.995	+1.291	+0.968	1.078	0.997	+1.495	+1.298
1–3	1.042	1.309	0.991	+3.262	+2.306	1.104	0.996	+3.783	+2.272
1–4	1.064	1.394	0.989	+5.230	+2.516	1.074	0.997	+6.081	+2.291
(b) $k = 1.00$									
1–2	1.018	1.190	0.990	+0.782	+0.968	1.078	0.994	+1.189	+1.298
1–3	1.042	1.309	0.984	+2.533	+2.306	1.104	0.992	+3.366	+2.272
1–4	1.064	1.394	0.979	+4.166	+2.516	1.074	0.994	+5.762	+2.291

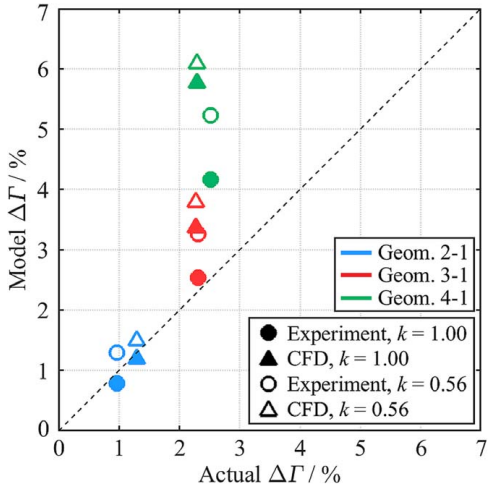

Fig. 27 Comparison of capacity changes predicted by the quasi-2D model and those determined by CFD and experiment

capacity change and hence improves the match with the measured vane capacity changes. The model performance is then very good for Geometry change 1–2 (under-predictions of −0.186% and −0.109% for experiment and CFD, respectively), reasonable for Geometry change 1–3 (over-predictions of +0.227% and +1.094% for experiment and CFD, respectively), and very poor for Geometry change 1–4 (over-predictions of +1.650% and +3.471% for experiment and CFD, respectively). These data are also plotted in Fig. 27, shown by solid circles and triangles.

Whether we take the empirically justified value of $k = 0.56$ from Fielding [2] or the limiting value of $k = 1.00$ for fully mixed loss, we see that the simple area-loss model cannot meaningfully reproduce the observed capacity changes for all geometries. The deteriorating performance of the model as the change in TE overhang length becomes greater is explained by increasing changes in aerodynamics not being included in the framework of the quasi-2D model. In general, the aerodynamic impact of a geometry change could be either positive or negative with respect to the model prediction (results of Fig. 27 and Table 9). This explains the relatively small sensitivity to the value of k and suggests that a model of this nature would be unlikely to give results applicable across a range of vane geometries.

References

[1] Afanasiev, I. V., Granovskiy, A. V., Karelin, A. M., and Kostege, M. K., 2004, "Effect of 3D Vane Shape on the Vane Capacity," Proceedings of ASME Turbo Expo 2004, Vienna, Jun. 14–17, Paper No. GT2004-53095.

[2] Fielding, L., 1981, "The Effect of Irreversibility on the Capacity of a Turbine Blade Row," Proc. Inst. Mech. Eng., **195**(1), pp. 127–137.

[3] Povey, T., Sharpe, M., and Rawlinson, A., 2011, "Experimental Measurements of Gas Turbine Flow Capacity Using a Novel Transient Technique," ASME J. Turbomach., **133**(1), p. 011005.

[4] Kirollos, B., Lubbock, R., Beard, P., Goenaga, F., Rawlinson, A., Janke, E., and Povey, T., 2017, "ECAT: An Engine Component Aerothermal Facility at the University of Oxford," Proceedings of ASME Turbo Expo 2017, Charlotte, NC, Jun. 26–30, Paper No. GT2017-64736.

[5] Burdett, D., Hambidge, C., and Povey, T., 2020, "Analysis of Ultra-Low Uncertainty Gas Turbine Flow Capacity Measurement Techniques," Proc. Inst. Mech. Eng. Part A: J. Power Energy., pp. 1–27.

[6] Kost, F., and Holmes, A., 1985, "Aerodynamic Effect of Coolant Ejection in the Rear Part of Transonic Rotor Blades," AGARD-CP-390, Heat Transfer and Cooling in Gas Turbine Blades, Paper 41.

[7] Uzol, O., and Camci, C., 2001, "Aerodynamic Loss Characteristics of a Turbine Blade With Trailing Edge Coolant Ejection: Part II—External Aerodynamics, Total Pressure Losses and Predictions," ASME J. Turbomach., **123**(2), pp. 249–257.

[8] Povey, T., 2010, "Effect of Film Cooling on Turbine Capacity," ASME J. Eng. Gas Turbines Power, **132**(1), p. 011901.

[9] Hambidge, C., and Povey, T., 2012, "Numerical and Analytical Study of the Effect of Film Cooling on HP NGV Capacity," Proceedings of ASME Turbo Expo 2012, Copenhagen, June 11–15, Paper No. GT2012-69066.

[10] Högner, L., Nasuf, A., Voigt, P., Voigt, M., Vogeler, K., Meyer, M., Berridge, C., and Goenaga, F., 2016, "Analysis of High Pressure Turbine Nozzle Guide Vanes Considering Geometric Variations," Proceedings of ASME Turbo Expo 2016, Seoul, June 13–17, Paper No. GT2016-57502.

[11] British Standards Institution, 2005, *BS EN ISO 9300:2005 Measurement of Gas Flow by Means of Critical Flow Venturi Nozzles*, British Standards Institution, London.

[12] Melzer, A. P., and Pullan, G., 2019, "The Role of Vortex Shedding in the Trailing Edge Loss of Transonic Turbine Blades," ASME J. Turbomach., **141**(4), p. 041001.

[13] Fielding, L., 2000, *Turbine Design: The Effect on Axial Flow Turbine Performance of Parameter Variation*, ASME Press, New York.

[14] Ainley, D. G., and Mathieson, G. C. R., 1951, *A Method of Performance Estimation for Axial Flow Turbines*, Aeronautical Research Council, London. No. ARC-R/M-2974.

[15] Dunham, J., and Came, P. M., 1970, "Improvements to the Ainley–Mathieson Method of Turbine Performance Prediction," ASME J. Eng. Power, **92**(3), pp. 252–256.